Implications of CTEQ global analysis for collider observables

Pavel M. Nadolsky,[1] Hung-Liang Lai,[2,3] Qing-Hong Cao,[4] Joey Huston,[1] Jon Pumplin,[1] Daniel Stump,[1] Wu-Ki Tung,[1,3] and C.-P. Yuan[1]

[1]*Department of Physics and Astronomy, Michigan State University, East Lansing, Michigan 48824-1116, USA*
[2]*Taipei Municipal University of Education, Taipei, Taiwan*
[3]*Department of Physics, University of Washington, Seattle, Washington 98105, USA*
[4]*Department of Physics and Astronomy, University of California at Riverside, Riverside, California 92521, USA*
(Received 18 March 2008; published 21 July 2008)

The latest CTEQ6.6 parton distributions, obtained by global analysis of hard-scattering data in the framework of general-mass perturbative QCD, are employed to study theoretical predictions and their uncertainties for significant processes at the Fermilab Tevatron and CERN Large Hadron Collider. The previously observed increase in predicted cross sections for the standard-candle W and Z boson production processes in the general-mass scheme (compared to those in the zero-mass scheme) is further investigated and quantified. A novel method to constrain parton distribution function (PDF) uncertainties in LHC observables, by effectively exploiting PDF-induced correlations with benchmark standard model cross sections, is presented. Using this method, we show that the $t\bar{t}$ cross section can potentially serve as a standard-candle observable for the LHC processes dominated by initial-state gluon scattering. Among other benefits, precise measurements of $t\bar{t}$ cross sections would reduce PDF uncertainties in predictions for single top-quark and Higgs boson production in the standard model and minimal supersymmetric standard model.

DOI: 10.1103/PhysRevD.78.013004 PACS numbers: 12.15.Ji, 12.38.Cy, 13.85.Qk

I. INTRODUCTION

Parton distribution functions (PDFs) are essential inputs required to make theoretical predictions for the CERN Large Hadron Collider (LHC) and other hadron scattering facilities. They are extracted from a comprehensive global analysis of hard-scattering data from a variety of fixed-target and collider experiments in the framework of perturbative QCD. Experimental groups envision an ambitious program to tightly constrain PDF degrees of freedom using the upcoming LHC data. Such constraints will not be feasible in the early runs of the LHC, when experimental systematic errors will typically be large, and the collider luminosity itself will not be known to better than 10–20%. Thus the experiments plan to perform real-time monitoring of the collider luminosity through the measurement of benchmark standard model cross sections, notably those for production of massive electroweak bosons [1–4]. These cross sections are large and can be measured fairly precisely soon after the LHC turn-on. To realize this goal, as well as to carry out the general physics program of the LHC, it is important, on one hand, to systematically explore the dependence of W, Z, and other ''standard-candle'' cross sections on the PDFs and other aspects of QCD theory; and, on the other hand, to establish and exploit *correlations* with these observables arising from the dependence on the universal parton distributions. These tasks must be carried out using the most up-to-date PDFs, with quantitative estimates of their uncertainties.

In a series of recent papers [5–7], we have extended the conventional CTEQ global PDF analysis [8,9] to incorporate a comprehensive treatment of heavy-quark effects and to include the most recent experimental data. The PDFs constructed in those studies consist of (i) the base set CTEQ6.5M, together with 40 eigenvector sets along 20 orthonormal directions in the parton parameter space [5], (ii) several PDF sets CTEQ6.5Sn ($n = -2, \ldots 4$), designed to probe the strangeness degrees of freedom under the assumption of symmetric or asymmetric strange sea [6], and (iii) several sets CTEQ6.5XCn ($n = 0 \ldots 6$) for a study of the charm sector of the parton parameter space, in particular, the allowed range of independent nonperturbative (''intrinsic'') charm partons in several possible models [7]. Some prominent physical consequences of these new PDFs compared to previous PDFs, particularly for W and Z production cross sections at hadron colliders, were pointed out in these papers.

The current paper pursues a more detailed exploration of the physical implications of our new generation of PDFs, particularly at the LHC. In the process of this detailed study, we found it desirable to expand and improve the CTEQ6.5 analysis on several fronts. The new general-purpose set of error PDFs, designated as CTEQ6.6, includes an independent strangeness parametrization constrained by the dimuon deep-inelastic scattering (DIS) data, in contrast to the CTEQ6.5 error PDF set, which assumed proportionality of the strangeness distribution to the sum of up and down antiquark PDFs. Improvements made in the numerical treatment of heavy-quark contributions to DIS cross sections lead to a better agreement of CTEQ6.6M predictions with the DIS heavy-flavor production data (F_2^c, F_2^b) as compared to CTEQ6.5M. The range of

x covered by the PDF parametrizations was extended to lower values, and the PDFs in the intrinsic charm framework were updated. The default values of the heavy-quark masses and QCD coupling strength are kept the same as in the CTEQ6.5 analysis ($m_c = 1.3$ GeV, $m_b = 4.5$ GeV, and $\alpha_s(M_Z) = 0.118$). In addition, we present the best-fit PDF parametrizations for alternative values of $m_c = 1.4$ GeV, $m_b = 4.75$ GeV, and $\alpha_s(M_Z) = 0.112$–0.125. All new results discussed in this paper are based on these improved PDFs.[1] They will be further described in Sec. III.

We make a systematic effort to address the quantitative challenges described in the first paragraph of this introduction. We study the impact of the new PDFs on the predicted cross sections for important physical processes at the LHC, with their associated uncertainty ranges. The PDF uncertainties in future measurements may behave at odds with initial intuitions because of rich connections between PDFs of different flavors and in different kinematical ranges arising from (a) physical symmetries, such as scale invariance and parton sum rules, and (b) experimental constraints. In some cases, notably in Z boson production at the LHC, the largest PDF uncertainty arises from less-constrained subleading scattering channels rather than from the well-known dominant subprocesses. In order to access such rich interconnections efficiently and completely, we introduce in Sec. II a quantitative measure of correlations existing between the PDFs and physical observables. The correlation analysis extends the Hessian method [8,10] to investigate pairwise relations between collider observables. This analysis is employed in Sec. IV as a tool to enhance the power of certain crucial phenomenological predictions, notably for W and Z boson production cross sections, and to examine the role of $t\bar{t}$ production as an additional standard-candle process. At the end of Sec. IV, we apply the gained knowledge to identify the main sources of PDF uncertainty in single-top production and in several processes for Higgs boson production in the standard model (SM) and minimal supersymmetric standard model (MSSM).

II. CORRELATIONS DUE TO PDFS

In many applications, it is instructive to establish whether a collider observable shares common degrees of freedom with precisely measured SM cross sections through the nonperturbative PDF parametrizations, a feature that can be exploited to predict the observable more reliably. In Sec. IV, we will explore such PDF-induced correlations between interesting collider cross sections. But first we will define the relevant theoretical framework.

Let X be a variable that depends on the PDFs. It can be any one of the physical quantities of interest, or even a PDF itself at some given (x, μ). We consider X as a function of the parameters $\{a_i\}$ that define the PDFs at the initial scale μ_0. Thus we have $X(\vec{a})$, where $\vec{a}$ forms a vector in an N-dimensional PDF parameter space, with N being the number of free parameters in the global analysis that determines these PDFs. In the Hessian formalism for the uncertainty analysis developed in [10] and used in all of our recent work, this parton parameter space is spanned by a set of orthonormal eigenvectors obtained by a self-consistent iterative procedure [5,8].

If $\vec{a}_0$ represents the best fit obtained with a given set of theoretical and experimental inputs, the variation of $X(\vec{a})$ for parton parameters $\vec{a}$ in the neighborhood of $\vec{a}_0$ is given, within the Hessian approximation, by a linear formula

$$\Delta X(\vec{a}) = X(\vec{a}) - X(\vec{a}_0) = \vec{\nabla} X|_{\vec{a}_0} \cdot \Delta\vec{a}, \tag{1}$$

where $\vec{\nabla} X$ is the gradient of $X(\vec{a})$, and $\Delta\vec{a} = \vec{a} - \vec{a}_0$. As explained in detail in Refs. [5,8,10], the uncertainty range of the PDFs in our global analysis is characterized by a tolerance factor T, equal to the radius of a hypersphere spanned by maximal allowed displacements $\Delta\vec{a}$ in the orthonormal PDF parameter representation. T is determined by the criterion that all PDFs within this tolerance hypersphere should be consistent with the input experimental data sets within roughly 90% C.L. The detailed discussions and the specific iterative procedure used to construct the eigenvectors can be found in Refs. [5,8,10].

In practice, the results of our uncertainty analysis are characterized by $2N$ sets of published eigenvector PDF sets along with the central fit. We have 2 PDF sets for each of the N eigenvectors, along the ($\pm$) directions, respectively, at the distance $|\Delta\vec{a}| = T$. The i-th component of the gradient vector $\vec{\nabla} X$ may be approximated by

$$\frac{\partial X}{\partial a_i} \equiv \partial_i X = \frac{1}{2}(X_i^{(+)} - X_i^{(-)}), \tag{2}$$

where $X_i^{(+)}$ and $X_i^{(-)}$ are the values of X computed from the two sets of PDFs along the ($\pm$) direction of the i-th eigenvector. The uncertainty of the quantity X due to its dependence on the PDFs is then defined as

$$\Delta X = |\vec{\nabla} X| = \frac{1}{2}\sqrt{\sum_{i=1}^{N}(X_i^{(+)} - X_i^{(-)})^2}, \tag{3}$$

where for simplicity we assume that the positive and negative errors on X are the same.[2]

We may extend the uncertainty analysis to define a *correlation* between the uncertainties of two variables, say $X(\vec{a})$ and $Y(\vec{a})$. We consider the projection of the tolerance hypersphere onto a circle of radius 1 in the plane

[1] The CTEQ6.6 PDFs represent improvements over their counterparts in CTEQ6.5, while preserving the same physics inputs. Therefore we recommend that CTEQ6.6 be the preferred PDFs to use in future phenomenology studies.

[2] A more detailed equation for ΔX accounts for differences between the positive and negative errors [9,11]. It is used for $t\bar{t}$ cross sections in Table II and Fig. 12.

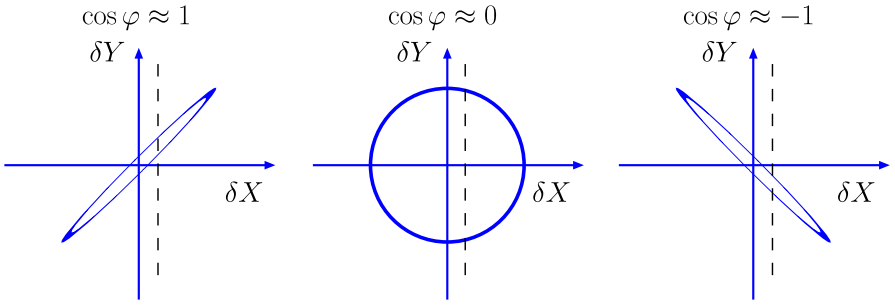

FIG. 1 (color online). Dependence of the correlation ellipse formed in the $\delta X - \delta Y$ plane on the value of $\cos\varphi$.

of the gradients $\vec{\nabla}X$ and $\vec{\nabla}Y$ in the parton parameter space [10,11]. The circle maps onto an ellipse in the XY plane. This "tolerance ellipse" is described by Lissajous-style parametric equations,

$$X = X_0 + \Delta X \cos\theta, \tag{4}$$

$$Y = Y_0 + \Delta Y \cos(\theta + \varphi), \tag{5}$$

where the parameter θ varies between 0 and 2π, $X_0 \equiv X(\vec{a}_0)$, and $Y_0 \equiv Y(\vec{a}_0)$. ΔX and ΔY are the maximal variations $\delta X \equiv X - X_0$ and $\delta Y \equiv Y - Y_0$ evaluated according to Eq. (3), and φ is the angle between $\vec{\nabla}X$ and $\vec{\nabla}Y$ in the $\{a_i\}$ space, with

$$\cos\varphi = \frac{\vec{\nabla}X \cdot \vec{\nabla}Y}{\Delta X \Delta Y} = \frac{1}{4\Delta X \Delta Y}\sum_{i=1}^{N}(X_i^{(+)} - X_i^{(-)})(Y_i^{(+)} - Y_i^{(-)}). \tag{6}$$

The quantity $\cos\varphi$ characterizes whether the PDF degrees of freedom of X and Y are correlated ($\cos\varphi \approx 1$), anticorrelated ($\cos\varphi \approx -1$), or uncorrelated ($\cos\varphi \approx 0$). If units for X and Y are rescaled so that $\Delta X = \Delta Y$ (e.g., $\Delta X = \Delta Y = 1$), the semimajor axis of the tolerance ellipse is directed at an angle $\pi/4$ (or $3\pi/4$) with respect to the ΔX axis for $\cos\varphi > 0$ (or $\cos\varphi < 0$). In these units, the ellipse reduces to a line for $\cos\varphi = \pm 1$ and becomes a circle for $\cos\varphi = 0$, as illustrated by Fig. 1. These properties can be found by diagonalizing the equation for the correlation ellipse,

$$\left(\frac{\delta X}{\Delta X}\right)^2 + \left(\frac{\delta Y}{\Delta Y}\right)^2 - 2\left(\frac{\delta X}{\Delta X}\right)\left(\frac{\delta Y}{\Delta Y}\right)\cos\varphi = \sin^2\varphi. \tag{7}$$

A magnitude of $|\cos\varphi|$ close to unity suggests that a precise measurement of X (constraining δX to be along the dashed line in Fig. 1) is likely to constrain tangibly the uncertainty δY in Y, as the value of Y shall lie within the needle-shaped error ellipse. Conversely, $\cos\varphi \approx 0$ implies that the measurement of X is not likely to constrain δY strongly.[3]

[3]The allowed range of $\delta Y/\Delta Y$ for a given $\delta \equiv \delta X/\Delta X$ is $r_Y^{(-)} \le \delta Y/\Delta Y \le r_Y^{(+)}$, where $r_Y^{(\pm)} \equiv \delta\cos\varphi \pm \sqrt{1-\delta^2}\sin\varphi$.

The parameters of the correlation ellipse are sufficient to deduce, under conventional approximations, a Gaussian probability distribution $P(X, Y|\text{CTEQ6.6})$ for finding certain values of X and Y based on the pre-LHC data sets included in the CTEQ6.6 analysis. If the LHC measures X and Y nearly independently of the PDF model, a new confidence region for X and Y satisfying both the CTEQ6.6 and LHC constraints can be determined by combining the prior probability $P(X, Y|\text{CTEQ6.6})$ with the new probability distribution $P(X, Y|\text{LHC})$ provided by the LHC measurement. For this purpose, it suffices to construct a probability distribution

$$P(X, Y|\text{CTEQ6.6 + LHC}) = P(X, Y|\text{CTEQ6.6}) \times P(X, Y|\text{LHC}), \tag{8}$$

which establishes the combined CTEQ6.6 + LHC confidence region without repeating the global fit.

The values of ΔX, ΔY, and $\cos\varphi$ are also sufficient to estimate the PDF uncertainty of any function $f(X, Y)$ of X and Y by relating the gradient of $f(X, Y)$ to $\partial_X f \equiv \partial f/\partial X$ and $\partial_Y f \equiv \partial f/\partial Y$ via the chain rule:

$$\Delta f = |\vec{\nabla} f| = \sqrt{(\Delta X \partial_X f)^2 + 2\Delta X \Delta Y \cos\varphi\, \partial_X f \partial_Y f + (\Delta Y \partial_Y f)^2}. \tag{9}$$

Of particular interest is the case of a rational function $f(X, Y) = X^m/Y^n$, pertinent to computations of various cross section ratios, cross section asymmetries, and statistical significance for finding signal events over background processes [11]. For rational functions Eq. (9) takes the form

$$\frac{\Delta f}{f_0} = \sqrt{\left(m\frac{\Delta X}{X_0}\right)^2 - 2mn\frac{\Delta X}{X_0}\frac{\Delta Y}{Y_0}\cos\varphi + \left(n\frac{\Delta Y}{Y_0}\right)^2}. \tag{10}$$

For example, consider a simple ratio, $f = X/Y$. Then $\Delta f/f_0$ is suppressed ($\Delta f/f_0 \approx |\Delta X/X_0 - \Delta Y/Y_0|$) if X and Y are strongly correlated, and it is enhanced ($\Delta f/f_0 \approx \Delta X/X_0 + \Delta Y/Y_0$) if X and Y are strongly anticorrelated.

As would be true for any estimate provided by the Hessian method, the correlation angle is inherently approximate. Equation (6) is derived under a number of simplifying assumptions, notably in the quadratic approximation for the χ^2 function within the tolerance hypersphere, and by using a symmetric finite-difference formula (2) for $\{\partial_i X\}$ that may fail if X is not monotonic. With these limitations in mind, we find the correlation angle to be a convenient measure of interdependence between quantities of diverse nature, such as physical cross sections and parton distributions themselves. For collider applications, the correlations between measured cross sections for crucial SM and beyond SM processes will be of primary interest, as we shall illustrate in Sec. IV. As a first example however, we shall present some representative results on correlations between the PDFs in the next section.

III. OVERVIEW OF CTEQ6.6 PDFS

A. CTEQ6.6 versus CTEQ6.1

The CTEQ6.5 PDFs [5–7] and their improved version CTEQ6.6 presented here are based on a new implementation of heavy-quark mass effects in perturbative QCD cross sections, realized in the Aivazis-Collins-Olness-Tung (ACOT) general-mass (GM) variable number scheme [12,13] and supplemented by more recent conceptual developments (SACOT [12,14] and ACOT-χ [15] approaches) introduced to simplify computations involving the heavy-quark mass and to treat adequately particle kinematics at energies close to the heavy-quark mass thresholds. A detailed discussion of the heavy-quark scheme employed in our work was published recently in Ref. [5]. The quality of the global analysis is further enhanced by the inclusion of newer data sets, replacement of structure functions $F_2(x, Q)$ and $F_3(x, Q)$ by the directly measured cross sections in H1 and ZEUS DIS data sets, relaxation of *ad hoc* constraints on the parametrization of strange quark PDFs, and improvements in the global fitting procedure. The CTEQ6.6 PDF set includes four additional PDF eigenvectors to accommodate the free strangeness parametrization, as described below. It is also in a better agreement with HERA charm production cross sections than CTEQ6.5. The public distributions, available at the LHAPDF depository [16], include a central PDF set, denoted as CTEQ6.6M, and 44 eigenvector sets that span the range of uncertainties in the parton parameter space due to input experimental errors.

Incorporation of the full heavy-quark mass effects in the general-mass formalism leads to the suppression of heavy-flavor contributions to the DIS structure functions $F_\lambda(x, Q)$ compared to the ordinary zero-mass (ZM) scheme. For neutral-currents $F_\lambda(x, Q)$, which dominate the global analysis, the suppressions occur in (a) the flavor-excitation partonic processes with incoming c and b quarks, through the rescaling of the light-cone momentum fraction variable, and (b) the light-flavor scattering processes involving explicit flavor creation (such as the gluon-photon fusion), through the mass dependence in the partonic cross section (Wilson coefficient) [5,15]. Since the theoretical calculations in the global fit must agree with the extensive DIS data at low and moderate Q, the reduction in c, b, and g contributions in the GM next-to-leading order (NLO) fit must be compensated by larger magnitudes of light-quark and antiquark contributions. One therefore expects to see an increase in the light-quark PDFs extracted in the GM scheme compared to those from ZM analyses in the appropriate (x, Q) region. This improvement leads to significant changes in some key predictions compared to the ZM formalism.

We illustrate the impact of the improved treatment of heavy-quark scattering by comparing predictions made using the CTEQ6.6 PDFs (realized in the GM scheme) and zero-mass CTEQ6.1 PDFs [9] (realized in the ZM scheme). All of the cross sections in our global analysis are calculated at NLO in perturbative QCD. Figures showing comparison of CTEQ6.6 and CTEQ6.1 for various PDF flavors are collected at [17]. Since these figures are rather similar to their counterparts comparing the CTEQ6.5 and CTEQ6.1 PDFs [5], we do not reproduce them in this paper, except for the strangeness and charm PDFs.

The most consequential differences between CTEQ6.6 and CTEQ6.1 PDFs for u and d quarks occur at $x \lesssim 10^{-3}$, cf. Ref. [17]. They can substantially affect predictions for quark-induced processes at the LHC, making the predicted cross sections larger by several percent (6–7% in W, Z production), as will be discussed in more detail in Sec. IV.

As a new feature, the CTEQ6.6 analysis allows the shape of strange quark distributions to be independent from the nonstrange sea distributions. We no longer impose the familiar ansatz $s(x, \mu_0) \propto \bar{u}(x, \mu_0) + \bar{d}(x, \mu_0)$, because the included dimuon DIS data ($\nu A \to \mu^+ \mu^- X$) [18] probes the strange quark distributions via the underlying process $sW \to c$, making the above ansatz unnecessary. However, as shown in Ref. [6], the existing experimental constraints on the strange PDFs remain relatively weak and have power to determine at most two new degrees of freedom associated with the strangeness in the limited range $x > 10^{-2}$. Thus in the CTEQ6.6 analysis we add two new free parameters characterizing the strange PDFs.[4] We continue to assume $s(x) = \bar{s}(x)$ in these fits, since the current data do not place statistically significant constraints on the difference between $s(x)$ and $\bar{s}(x)$ [6].

At $x \lesssim 10^{-2}$, the available data probe mostly a combination $(4/9)[u(x) + \bar{u}(x)] + (1/9)[d(x) + \bar{d}(x) + s(x) + \bar{s}(x)]$ accessible in neutral-current DIS, but not the detailed flavor composition of the quark sea. The shape of $s(x, \mu_0)$ at very small x can vary over a large range, accompanied by

[4]Assignment of more than two free strangeness parameters does not tangibly improve the quality of the fit and creates undesirable flat directions in the Hessian eigenvector space [6].

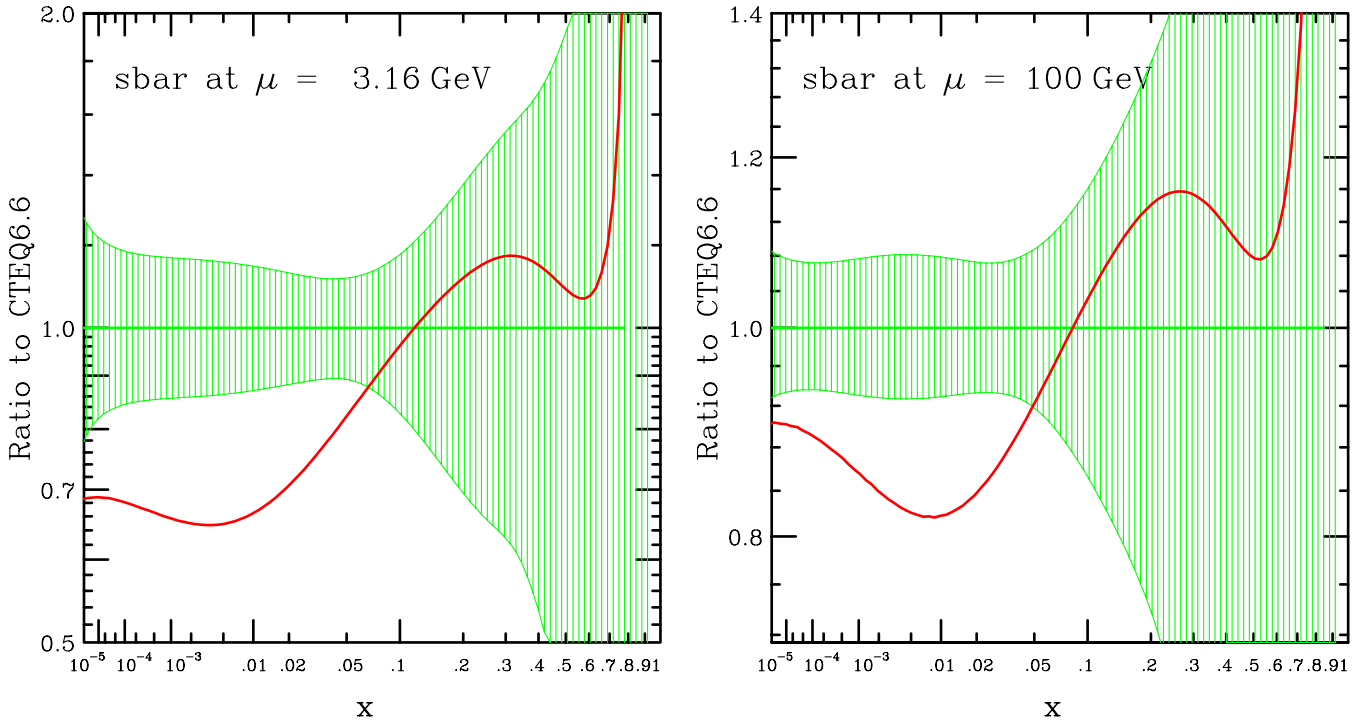

FIG. 2 (color online). CTEQ6.6 PDF uncertainty bands (green shaded area) and CTEQ6.1M PDF (red solid line) for $s = \bar{s}$ at factorization scales $\mu = 3.16$ and 100 GeV.

corresponding adjustments in the other sea quark flavors. In other words, the strangeness to nonstrangeness ratio at small x, $R_s = \lim_{x\to 0}[s(x, \mu_0)/(\bar{u}(x, \mu_0) + \bar{d}(x, \mu_0))]$, is entirely unconstrained by the data. But, on general physics grounds, one would expect this ratio to be of order 1 (or, arguably, a bit smaller). Thus, in the current CTEQ6.6 analysis, we adopt a parametrization for the strange PDF of the form $s(x, \mu_0) = A_0 x^{A_1}(1 - x)^{A_2} P(x)$, where A_1 is set equal to the analogous parameter of $\bar{u}$ and $\bar{d}$ based on Regge considerations. A smooth function $P(x)$ (of a fixed form for all 45 CTEQ6.6 PDF sets) is chosen to ensure that the ratio R_s stays within a reasonable range. There is considerable freedom in the choice of $P(x)$, and that is a part of the theoretical uncertainty associated with any parametrization of the initial PDFs.[5] Fig. 2 shows the CTEQ6.6 uncertainty bands of $\bar{s}(x, \mu)$ at two values of μ, along with the corresponding CTEQ6.1M PDFs. The values of R_s for the 44 eigenvector sets in this PDF series span 0.63–1.15.

Since the PDFs are *de facto* used for ultra-high-energy and astrophysics applications at $x < 10^{-5}$, the CTEQ6.6 PDFs are tabulated down to $x = 10^{-8}$ to provide numerically stable PDF values obtained by QCD evolution from parametrized initial parton distributions in this extreme x region. At the initial scale μ_0, the PDFs are extrapolated into the region $x < 10^{-5}$, not covered by the fitted data, by a Regge-like functional form proportional to x^a, where the negative parameter a is found from the fit at $x > 10^{-5}$. At larger μ scales, the PDFs are predicted from the initial condition at $\mu = \mu_0$ based on the NLO Dokshitzer-Gribov-Lipatov-Altarelli-Parisi (DGLAP) evolution. No extra dynamical effects that may be significant at small x are included in this parametrization.

B. Fits with nonperturbative charm

In the general-purpose CTEQ6.6 PDFs, we assume there is no nonperturbative intrinsic charm (IC), so that $c(x, \mu_0) = \bar{c}(x, \mu_0) = 0$ at the initial evolution scale $\mu_0 = m_c = 1.3$ GeV. To facilitate studies of the effect of possible IC, we have also created fits in which various amounts of IC (with $c = \bar{c}$) are assumed. These fits amount to updated versions of the light-cone motivated [19] and the sealike models for the shape of the input charm PDF discussed in [7]. For each IC model, we provide two PDF parameterizations with moderate and strong IC contributions, corresponding to charm quarks carrying 1% and 3.5% of the parent nucleon's momentum at $\mu = m_c$, respectively. Figure 3 shows that the assumption of IC can substantially increase the amount of $c = \bar{c}$ at factorization scales as large as 100 GeV.

C. Correlations

As mentioned before, correlations can be computed for any variables, including the PDFs themselves. The x and μ

[5]The theoretical uncertainty associated with the small-x quark flavor composition is generally larger than the Hessian uncertainty bands due to propagation of experimental errors for a given $P(x)$.

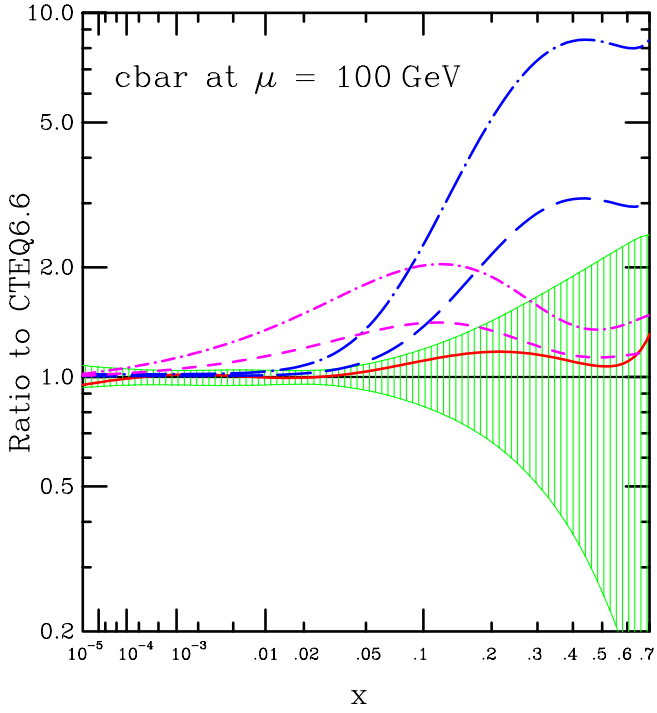

FIG. 3 (color online). CTEQ6.6 PDF uncertainty band for $c = \bar{c}$ with radiatively generated charm only (green shaded area) and PDFs with intrinsic charm: light-cone motivated form with moderate (long-dashed line) and strong (long-dash-dotted line) IC; sealike form with moderate (short-dashed line) and strong (short-dash-dotted line) IC. The red solid line is for CTEQ6.1M PDF. A factorization scale $\mu = 100$ GeV is assumed.

dependence of the PDF-PDF correlations provides broad insights about theoretical and experimental constraints affecting physical cross sections. To explore this dependence, we present contour plots of the correlation cosine $\cos\varphi$ for pairs of PDFs $f_{a_1}(x_1, \mu_1)$ and $f_{a_2}(x_2, \mu_2)$ at scales $\mu_{1,2} = 2$ and 85 GeV, plotted as a function of momentum fractions x_1 and x_2. A few such plots relevant for the ensuing discussion are shown in Fig. 4. A complete set of the contour plots in color and gray scale versions is available at [20].

Light (dark) shades of the gray color in Fig. 4 correspond to magnitudes of $\cos\varphi$ close to 1 (-1), as indicated by the legend. Several interesting patterns of the PDF correlations can be generally observed. First, consider self-correlations, in which the correlation cosine is formed between two values of the same PDF ($a_1 = a_2$, $\mu_1 = \mu_2$) evaluated at momentum fractions x_1 and x_2. The examples include the $u - u$, $g - g$, and $c - c$ correlations at $\mu_1 = \mu_2 = 85$ GeV shown in Figs. 4(a)–4(c).

Each self-correlation plot includes a trivial correlation, $\cos\varphi \approx 1$, occurring when x_1 and x_2 are about the same. This correlation occurs in light-colored areas along the $x_1 = x_2$ diagonals in Figs. 4(a)–4(c), of the shape that depends on the flavor of the PDF and the associated μ scale.

In the case of an up quark (Fig. 4(a)), the trivial correlation is the only pronounced pattern visible in the contour plot. The gluon PDF (Fig. 4(b)) and related c, b PDFs (Fig. 4(c)) show an additional strong anticorrelation in the vicinity of $(x_1, x_2) \approx (0.2, 0.01)$ arising as a consequence of the momentum sum rule. Important implications of this anticorrelation will be discussed in Sec. IV.

The gluon-strangeness correlation in Fig. 4(d) illustrates some typical patterns encountered in the case of sea partons. The gluons show a correlated behavior with strange quarks (and generally, sea quarks) at $x < 10^{-4} - 10^{-3}$ as a reflection of the singlet evolution (a light area in the lower left corner). The gluon PDF is anticorrelated with the strangeness PDF at $x_1 \sim 0.1$, $x_2 < 0.01$ because of the momentum sum rule (a dark area at the bottom). This anticorrelation significantly affects predictions for W and Z cross sections at the LHC. More complicated (and not so well-understood) patterns occur at $x_{1,2} > 0.3$, where the sea-parton behavior is less constrained by the data. Other types of correlation patterns, associated with the sum rules, perturbative evolution, and constraints from the experimental data, can be observed in the full set of contour plots [20].

IV. IMPLICATIONS FOR COLLIDER EXPERIMENTS

Soon after its turn-on, the LHC will provide vast samples of data in well-understood scattering processes at the electroweak scale, notably production of massive weak bosons $W^{\pm}$ and Z^0. These data will facilitate useful experimental calibrations, as well as measurements of the LHC luminosity and PDFs, with tentative experimental accuracy of about 1% [1–3]. To utilize such measurements of standard-candle cross sections most productively, one must understand *how* they constrain PDF degrees of freedom. It is necessary to explore how the predicted cross sections change due to improvements in the theoretical model, such as the transition from the zero-mass to general-mass factorization scheme, as well as due to the remaining freedom in the PDF parameters allowed by the data in the global fit.

In this section, we examine the quantitative connections between the PDFs and physical observables by applying the correlation analysis introduced in Sec. II. Since only large correlations (or anticorrelations) will be useful for practical purposes, we concentrate on pairs of cross sections characterized by large magnitudes of the correlation cosine, chosen in this paper to be $|\cos\varphi| > 0.7$. Overall dependence on the heavy-quark scheme is explored in Sec. IV A. A focused study of total inclusive cross sections is presented for W, Z, top-quark, and Higgs boson production in Secs. IV B, IV C, and IV D. The total cross sections are computed at the NLO in the QCD coupling strength α_s, using W boson mass $M_W = 80.403$ GeV, Z boson mass $M_Z = 91.1876$ GeV, and top-quark mass $m_t = 171$ GeV.

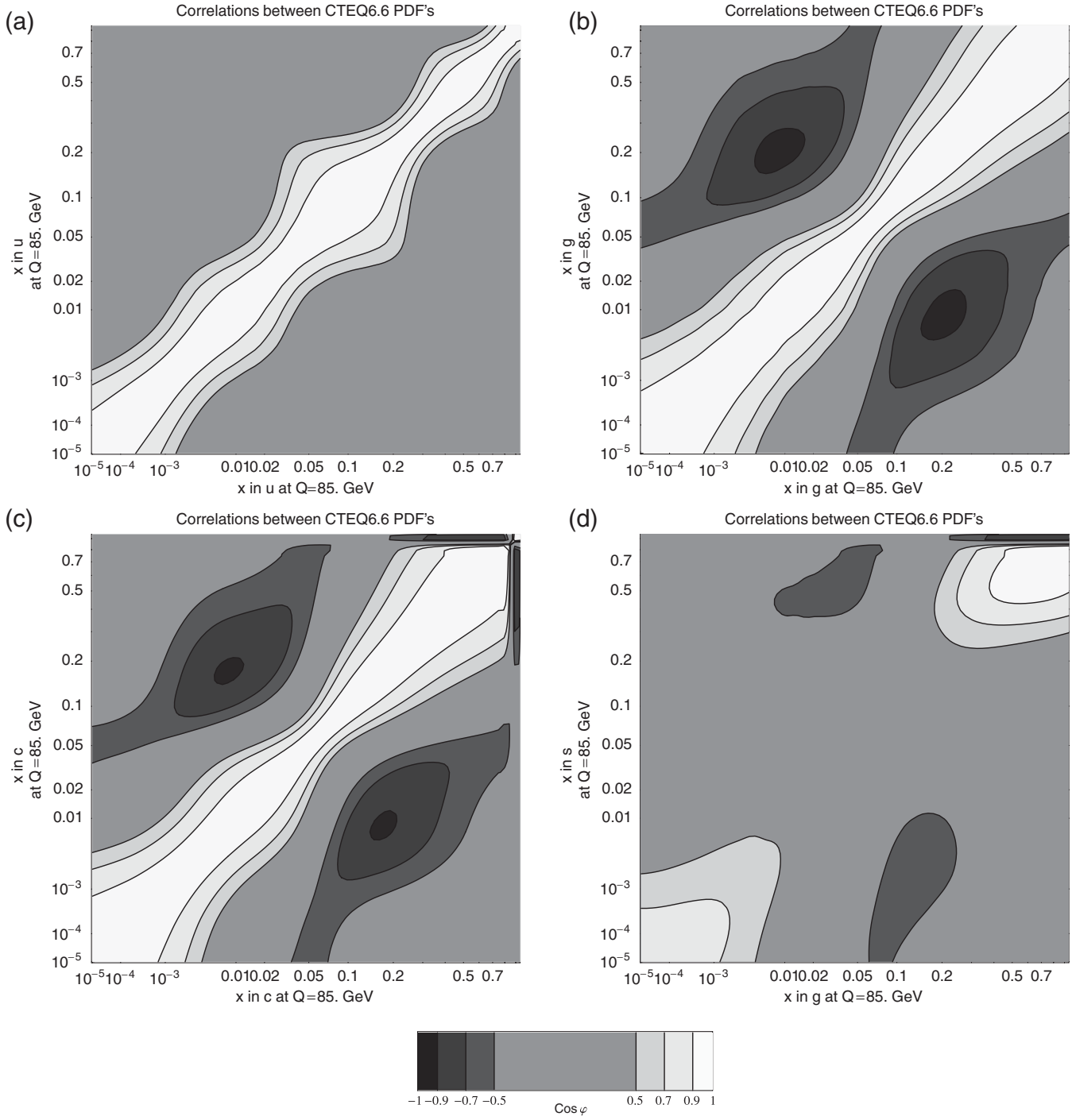

FIG. 4. Contour plots of correlations $\cos\varphi$ between two PDFs $f_1(x_1, \mu)$ and $f_2(x_2, \mu)$ at $\mu = 85$ GeV: (a) $u - u$; (b) $g - g$; (c) $c - c$; (d) $s - g$. Both axes are scaled as $x^{0.2}$.

In all calculations, both the renormalization and factorization scales are set to be equal to the mass of the final-state heavy particle, unless specified otherwise. The results presented below are representative of generic patterns observed in the PDF dependence of the studied cross sections. They depend weakly on theoretical assumptions about the quark flavor composition at small x discussed in Sec. III.

The LHC collaborations intend to measure ratios of LHC cross sections to standard candle (especially W and Z) cross sections. If two cross sections X and Y share common systematics, both experimental and theoretical, the systematic uncertainties partially cancel in the ratio $r = X/Y$. This cancellation is especially important in the first year or two of the LHC running, when the collider luminosity will only be known to the order of 10–20%.

Eventually the LHC ratios can provide important precision tests of the standard model, such as a precise measurement of the W boson mass from the ratio of W and Z total cross sections [21–24].

The PDF uncertainty on r is reduced ($\Delta r/r \approx |\Delta X/X - \Delta Y/Y|$) if X and Y are strongly correlated, cf. Equation (10). It is enhanced ($\Delta r/r \approx \Delta X/X + \Delta Y/Y$) if X and Y are strongly anticorrelated. It is therefore beneficial to construct the cross section ratios from pairs of correlated cross sections to reduce the PDF uncertainties. We will examine a ratio between the highly correlated W and Z total cross sections in Sec. IV B 3. We will also explore the inclusive $t\bar{t}$ production cross section, potentially useful for building ratios when an anticorrelation with W and Z cross sections occurs. W, Z, $t\bar{t}$ total cross section values for 45 CTEQ6.6 sets suitable for the computation of various PDF correlations can be downloaded at [17].

Leading channels for neutral Higgs boson (h^0) production in the standard model [25] are also investigated, including gluon-gluon fusion $gg \to h^0$, the dominant Higgs production mechanism; vector boson fusion (VBF) $q\bar{q} \to WW \to h^0$ or $q\bar{q} \to ZZ \to h^0$, a prominent channel employed at the LHC for both discovery and measurement of h^0WW (or h^0ZZ) couplings; and associated production of Higgs boson with a massive weak boson, $q\bar{q} \to Wh^0$ ($q\bar{q} \to Zh^0$), the leading discovery mode for Higgs masses $m_h < 200$ GeV at the Tevatron.

In addition, Higgs production channels in MSSM are considered: neutral CP-even or CP-odd Higgs boson production via bottom-quark annihilation, $b\bar{b} \to h$ ($h = h^0$, H^0, A^0) [26]; charged Higgs boson production via s, c, b scattering, $c\bar{s} + c\bar{b} \to h^+$ [27]; and associated production $q\bar{q}' \to W \to Ah^\pm$ of CP-odd (A) and charged Higgs bosons [28,29], with Higgs masses related as $m^2_{h^\pm} = m^2_A + M^2_W$ at the Born level. The $b\bar{b} \to h$ and $c\bar{s} + c\bar{b} \to h^+$ cross sections may be greatly enhanced if the ratio $\tan\beta = v_u/v_d$ of vacuum expectation values for up- and down-type Higgs doublets is of order 10 or more, a possibility that remains compatible with LEP, Tevatron, and other constraints [30]. To be specific, we evaluate $q\bar{q}h$ couplings at the tree level and choose effective $\tan\beta = 50$; but most of our results (presented as cross section ratios for different PDF sets and correlation cosines) are independent of the $\tan\beta$ value.

Supersymmetric neutral Higgs production $b\bar{b} \to h$ is sensitive largely to $b(x, \mu)$ and $g(x, \mu)$, while charged Higgs production probes a combination of $s(x, \mu)$, $c(x, \mu)$, and $b(x, \mu)$. Long-distance hadronic functions entering these processes require the general-mass scheme approach [6,7,31,32]. In hard-scattering inclusive cross sections, heavy-flavor mass corrections enter through ratios $m^2_{c,b}/p^2_i$ and are suppressed at large momentum scales $p^2_i \gg m^2_{c,b}$. We therefore neglect the charm and bottom-quark masses in hard-scattering matrix elements at TeV energies, while keeping the mass effects inside the PDFs.

A. Total cross sections at the Tevatron and the LHC

To discuss common differences between the general-mass (CTEQ6.6) and zero-mass (CTEQ6.1) predictions, we compute several total cross sections sensitive to light-quark, gluon, or heavy-quark scattering using the NLO programs WTTOT [33] and MCFM [34–36]. Figure 5 shows several CTEQ6.6 and CTEQ6.1 total cross sections and their PDF uncertainties at the $p\bar{p}$ collider Tevatron ($\sqrt{s} = 1.96$ TeV) and the pp Large Hadron Collider ($\sqrt{s} = 14$ TeV). They are plotted as ratios to CTEQ6.6M predictions. We do not show predictions for the CTEQ6.5 set, as those agree with CTEQ6.6 within the uncertainties.

The processes shown in the figure for the Tevatron occur at relatively large momentum fractions x, where CTEQ6.6 and CTEQ6.1 PDFs agree well. Consequently the CTEQ6.6 and CTEQ6.1 cross sections for the Tevatron processes coincide within the PDF uncertainties, as illustrated in Fig. 5(a). The magnitudes of the PDF uncertainties also remain about the same.

At the LHC (Fig. 5(b)), CTEQ6.6 cross sections for W and Z boson production are enhanced by 6–7% compared

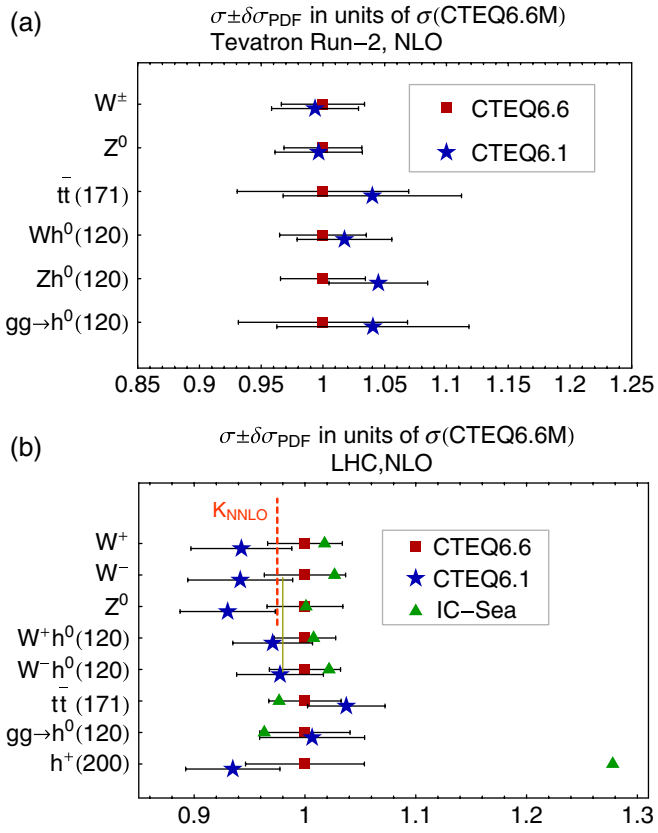

FIG. 5 (color online). Representative CTEQ6.6 (red boxes) and 6.1 (blue stars) total cross sections and PDF uncertainties at (a) the Tevatron and (b) LHC, normalized to the CTEQ6.6M cross section. Green triangles indicate CTEQ6.6 cross sections obtained under the assumption of a strong sealike intrinsic charm production (IC-Sea-3.5%).

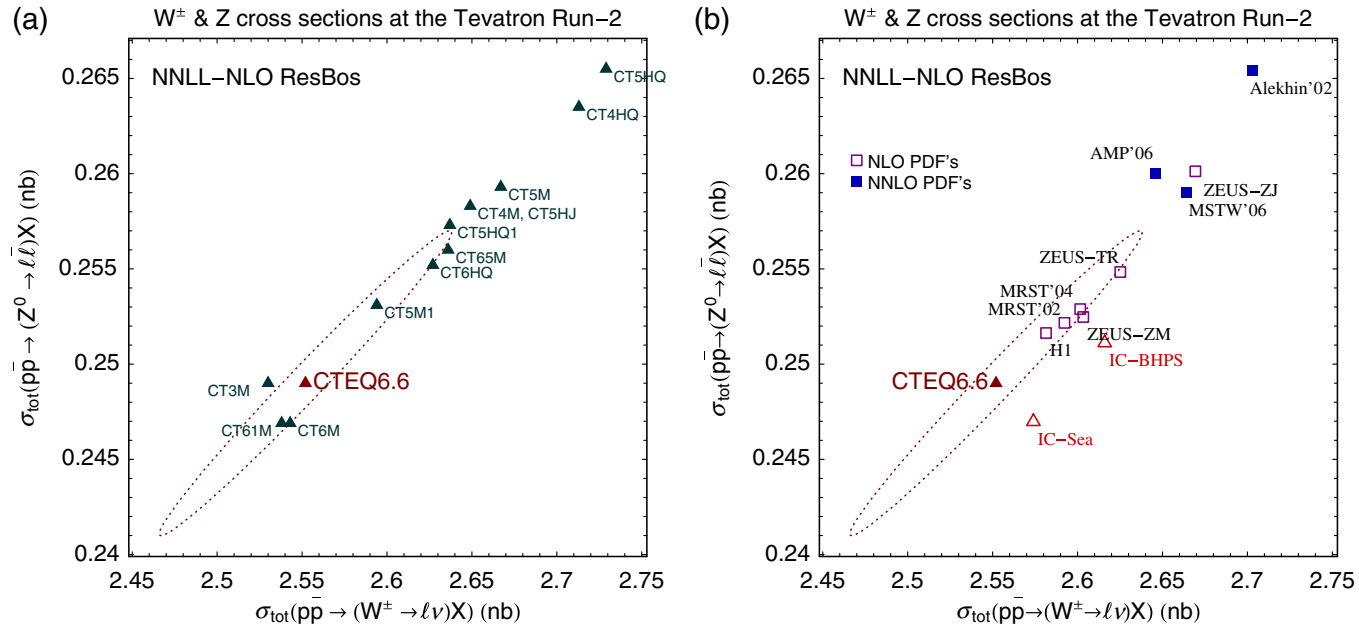

FIG. 6 (color online). CTEQ6.6 NNLL-NLO $W^{\pm}$ and Z production cross sections in the Tevatron Run-2, compared with predictions for other PDF sets by (a) CTEQ and (b) other groups.

to CTEQ6.1 because of the larger magnitudes of $\overset{(-)}{u}(x, Q)$ and $\overset{(-)}{d}(x, Q)$ in the relevant range of $x \sim M_{W,Z}/\sqrt{s} = 10^{-3}$–$10^{-2}$. The CTEQ6.6 light-quark parton luminosities $\mathcal{L}_{q_i\bar{q}_j}(x_1, x_2, Q) = q_i(x_1, Q)\bar{q}_j(x_2, Q)$ (and therefore CTEQ6.6 cross sections) are larger at such x by $2\delta f \approx 6\%$, where $\delta f \approx 3\%$ is the typical increase in the GM light-quark PDFs compared to the ZM PDFs. The Hessian PDF error obtained by our standard 90% C.L. criterion has decreased from 4.5–5% in CTEQ6.1 to 3.5% in CTEQ6.6, mostly because new DIS experimental data were included in the CTEQ6.6 fit. The differences between CTEQ6.6 and CTEQ6.1 exceed the magnitude of the NNLO correction to W and Z cross sections of the order 2% [37–40], indicated by a dashed line. Uncertainties of this size have important implications for the calibration of the LHC luminosity.

Other cross sections dominated by light-(anti)quark scattering at $x \sim 10^{-2}$ increase by comparable amounts. For example, the CTEQ6.6 cross sections for associated $W^{\pm}h$ or Z^0h boson production exceed CTEQ6.1 cross sections by 3–4%. In contrast, in processes dominated by gluon or heavy-quark scattering, such as $t\bar{t}$ production or $gg \to h^0X$, the general tendency for the CTEQ6.6 cross sections is to be a few percent lower compared to CTEQ6.1. The CTEQ6.6M $c\bar{s} + c\bar{b} \to h^+$ cross section is enhanced with respect to CTEQ6.1M by its larger strangeness PDF (cf. Fig. 2), despite some suppression of the $c\bar{b}$ contribution to this process. The LHC cross sections in Fig. 5(b) may change substantially if a fraction of charm quarks is produced through the nonperturbative intrinsic mechanism. For example, the rate for production $sc + sb \to h^{\pm}$ of MSSM charged Higgs bosons with mass 200 GeV would increase by 30% if sealike intrinsic charm contributions carry 3.5% of the parent nucleon's momentum, the maximal amount tolerated in the fit.

B. W and Z boson production cross sections

1. CTEQ6.6 vs other PDF sets

Large groups of collider cross sections, notably those dominated largely by quark scattering or largely by gluon scattering, exhibit correlated dependence on PDFs. Production of charged $W^{\pm}$ and neutral Z^0 bosons are essential quark-quark scattering processes that show such correlations.

Figures 6 and 7 summarize predictions for the total cross sections σ of W and Z production, obtained in the NNLL-NLO resummation calculation (of the order $\mathcal{O}(\alpha_s)$ + leading higher-order logarithms) [41–43] and using recent PDF sets by CTEQ [5,8,9,44–48], Alekhin/AMP [49,50], H1 [51], MRST/MSTW [52–55], and ZEUS [56,57] groups. We include decays of the massive bosons into lepton pairs in the improved Born approximation [42,58]. To provide a visual measure of the PDF uncertainty, each figure shows an error ellipse corresponding to our usual tolerance criterion.[6] The ellipses are found from Eqs. (4) and (5), using the parameters listed in Table I.

At the Tevatron, the CTEQ6.6 cross sections lie close to the CTEQ6.1 and CTEQ6.5 predictions (Fig. 6(a)), i.e., the dependence on the heavy-flavor scheme is relatively weak

[6]In two-dimensional plots, this criterion corresponds to a probability somewhat smaller than 90%.

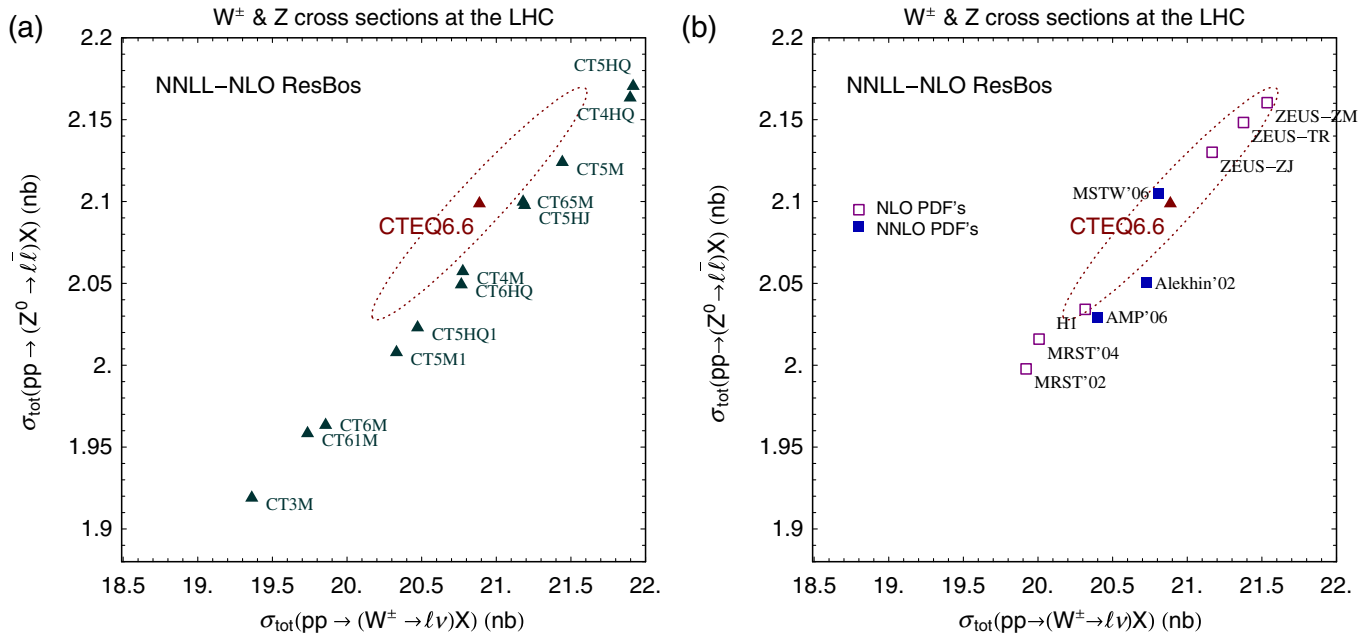

FIG. 7 (color online). CTEQ6.6 NNLL-NLO $W^{\pm}$ and Z production cross sections in the LHC, compared with predictions for (a) different PDF sets by CTEQ and (b) other groups.

in this case. The CTEQ6.6 cross sections agree well with predictions based on the PDF sets by the other groups (Fig. 6(b)).

At the LHC, the general-mass CTEQ6.6 cross sections exceed the zero-mass CTEQ6.1 cross sections by 6–7%, as shown in Fig. 7(a). The CTEQ6.6 and 6.5 Z^0 cross sections are about the same. The CTEQ6.6 $W^{\pm}$ cross section is somewhat smaller than the CTEQ6.5 cross section and does not lie on the same line in the $W - Z$ plane as the previous CTEQ sets. The predictions based on the latest CTEQ6.6, MSTW'06, and AMP'06 PDFs agree within 3% (Fig. 7(b)).

The total cross sections shown here are somewhat affected by higher-order contributions, not included under the current NNLL-NLO approximation. A prediction of *absolute* magnitudes of W and Z cross sections with 1% accuracy would require us to simultaneously evaluate NNLO QCD contributions of the order $\mathcal{O}(\alpha_s^2)$ [37–40] and NLO electroweak contributions of the order $\mathcal{O}(\alpha_s \alpha_{\rm EW})$ [59–67] for both the hard cross sections and PDFs, including all relevant spin correlations [68,69]. This level of accuracy is not yet achieved. However, the higher-order terms rescale the NLO hard cross sections by overall factors with weak dependence on the PDFs [39,40]. Therefore our NLO-NNLL total cross sections should reasonably estimate true *relative* differences caused by the PDFs.

The NNLL-NLO cross sections for AMP'2006 and MSTW'2006 are computed using the NNLO PDFs, since the NLO PDFs for these sets are not available. Such a combination is acceptable at the order we are working. For example, mixing of NLO-NNLL and NNLO orders is of little consequence in the case of the MRST'2004 set, for which the replacement of the NLO PDFs by the NNLO

TABLE I. Total cross sections σ, PDF-induced errors $\Delta\sigma$, and correlation cosines $\cos\varphi$ for Z^0, $W^{\pm}$, and $t\bar{t}$ production at the Tevatron Run-2 (Tev2) and LHC, computed with CTEQ6.6 PDFs.

$\sqrt{s}$ (TeV)	Scattering process	σ, $\Delta\sigma$ (pb)	Correlation $\cos\varphi$ with Z^0 (Tev2)	$W^{\pm}$ (Tev2)	Z^0 (LHC)	$W^{\pm}$ (LHC)
1.96	$p\bar{p} \to (Z^0 \to \ell^+\ell^-)X$	241(8)	1	**0.987**	0.23	0.33
	$p\bar{p} \to (W^{\pm} \to \ell\nu_\ell)X$	2560(40)	**0.987**	1	0.27	0.37
	$p\bar{p} \to t\bar{t}X$	7.2(5)	−0.03	−0.09	−0.52	−0.52
14	$pp \to (Z^0 \to \ell^+\ell^-)X$	2080(70)	0.23	0.27	1	**0.956**
	$pp \to (W^{\pm} \to \ell\nu)X$	20 880(740)	0.33	0.37	**0.956**	1
	$pp \to (W^+ \to \ell^+\nu_\ell)X$	12 070(410)	0.32	0.36	**0.928**	**0.988**
	$pp \to (W^- \to \ell^-\bar{\nu}_\ell)X$	8810(330)	0.33	0.38	**0.960**	**0.981**
	$pp \to t\bar{t}X$	860(30)	−0.14	−0.13	**−0.80**	**−0.74**

PDFs changes the cross sections by about 1.5%. Variations of this magnitude are clearly permissible until a more precise computation is fully developed.

2. Correlations between W, Z cross sections and PDFs

Although strong PDF-induced correlations between the W and Z cross sections are observed at both colliders, the mechanism driving these correlations at the LHC is not the same as at the Tevatron. The essential point is that, although the weak bosons are mostly produced in u and d quark-antiquark scattering, this dominant process may contribute little to the PDF uncertainty because of tight constraints imposed on the up- and down-quark PDFs by the DIS and Drell-Yan data.

Instead, a substantial fraction of the PDF uncertainty at the LHC (but not at the Tevatron) is contributed by sizable, yet less-constrained, contributions from heavy-quark (s, c, b) scattering. Subprocesses with initial-state s, c, and, to a smaller extent, b and g partons deliver up to 20% of the NLO rate at the LHC, compared to 2–4% at the Tevatron. All these partons are correlated with the gluons via DGLAP evolution, so that the LHC W and Z cross sections are particularly sensitive to the uncertainty in the gluon PDF. Consequently, W and Z cross sections at the LHC are better correlated with processes dominated by gluon scattering in the comparable kinematical range and not necessarily with u and d quark scattering, in striking contrast to the Tevatron.

To illustrate this point, Fig. 8 shows correlation cosines ($\cos\varphi$) between the W, Z cross sections and PDFs $f_a(x, Q)$ of different flavors, evaluated as functions of the momentum fraction x at $Q = 85$ GeV. The largest correlations between the cross section and PDFs occur at momentum

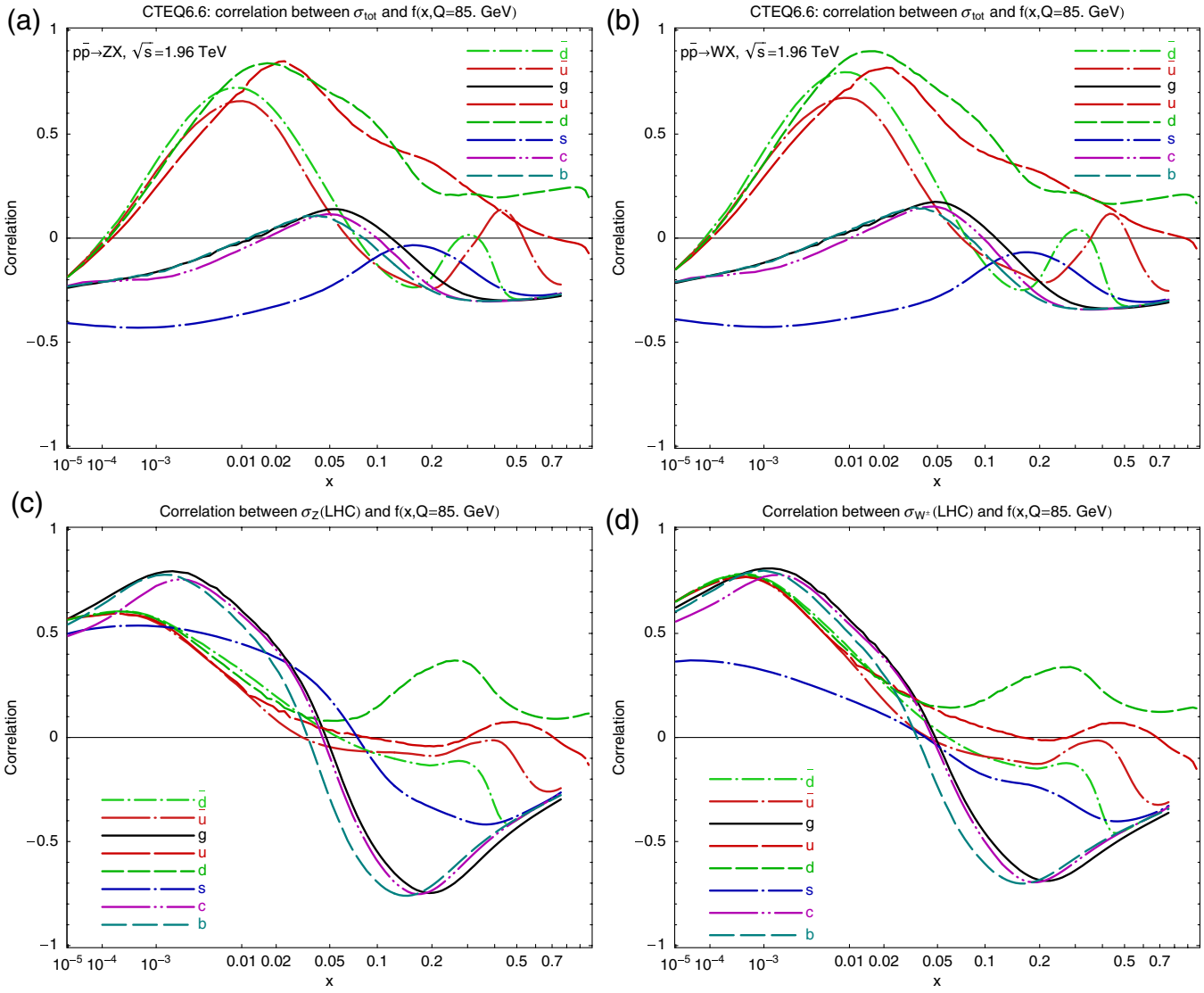

FIG. 8 (color online). (a,b) Correlation cosine ($\cos\varphi$) between the total cross sections for Z^0 and $W^{\pm}$ production at the Tevatron and PDFs, plotted as a function of x for $Q = 85$ GeV; (c,d) the same for the LHC.

fractions x of the order $M_{W,Z}/\sqrt{s}$ corresponding to central rapidity production, i.e., at $x \sim 0.04$ at the Tevatron and 0.006 at the LHC. PDF flavors with a very large correlation are associated with the major part of the PDF uncertainty in the physical cross section. Additional constraints on this flavor would help reduce the PDF uncertainty.

At the Tevatron Run-2 (Figs. 8(a) and 8(b)), large correlations exist with u, $\bar{u}$, d, and $\bar{d}$ PDFs, with $\cos\varphi$ reaching 0.95. No tangible correlation occurs with PDFs for s, c, b (anti)quarks and gluons.

At the LHC (Figs. 8(c) and 8(d)), the largest correlations are driven by charm, bottom, and gluon PDFs, followed by smaller correlations with u, d, and s quarks. The correlation with the u and d PDFs is reduced, although not entirely eliminated. A large correlation with the gluon at $x \sim 0.005$ is accompanied by a large anticorrelation ($\cos\varphi \sim -0.8$) with the gluon at $x \sim 0.1$–0.2, as a consequence of nucleon momentum conservation (cf. Sec. III C). This feature implies that the LHC W, Z cross sections are strongly anticorrelated with new particle production in gluon or heavy-quark scattering in the TeV mass range, and moderately anticorrelated with $t\bar{t}$ production (cf. Sec. IV C 2).

3. Impact of strangeness

We stress that the large correlation between the LHC Z cross section and the gluon distribution is generated primarily by the sizable $s\bar{s}$ scattering contribution, and not by a smaller qg scattering contribution. Similarly, a large correlation in W boson production is driven for the most part by the $c\bar{s}$ contribution. Yet the correlations of Z and W cross sections with the strangeness PDF, taken on its own, are rather small (see Figs. 8(c) and 8(d)). Adjustments in $s(x, Q)$ can be easily compensated by other quark PDFs without changing the physical W and Z cross sections. This extra freedom is absent in the case of the gluon PDF, since it affects all sea PDFs at once through perturbative evolution.

On the other hand, the ratio $r_{ZW} \equiv \sigma_Z/(\sigma_{W^+} + \sigma_{W^-})$ of the Z^0 and $W^\pm$ cross sections is very sensitive to the uncertainty in strangeness. Nominally r_{ZW} is an exemplary standard-candle LHC observable because of the cancellation of uncertainties inside the ratio. The CTEQ6.6 prediction $r_{ZW} = 0.100 \pm 0.001$ is in an excellent agreement with the predictions based on the other recent PDF sets. This result can be derived from Eq. (10) by substituting the correlated parameters of the W and Z cross sections in Table I.

Figure 9 indicates that r_{ZW} is mostly correlated with the strangeness PDF $s(x, Q)$ in the region $0.01 < x < 0.05$. It is anticorrelated with $\overset{(-)}{u}$ and $\overset{(-)}{d}$ at $x \sim 10^{-3}$. There is no tangible correlation with the gluon, charm, and bottom PDFs.

Since the strangeness is the least constrained distribution among the light-quark flavors [6,53,70], it is thus important to correctly model its uncertainty to estimate r_{ZW}.

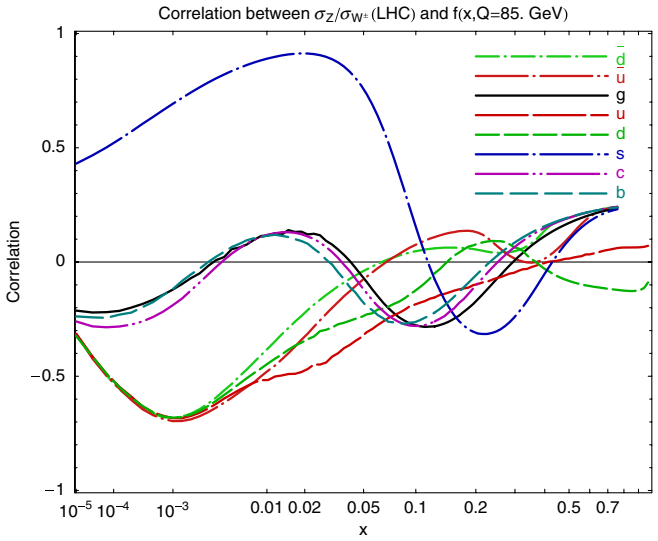

FIG. 9 (color online). Correlation cosine ($\cos\varphi$) between the ratio σ_Z/σ_W of LHC total cross sections for Z^0 and $W^\pm$ production at PDFs of various flavors, plotted as a function of x for $Q = 85$ GeV.

CTEQ6.6 is our first general-purpose PDF set that includes an independent parametrization for strangeness. It predicts a larger uncertainty in $s(x, Q)$ (hence, a larger Δr_{ZW}) than the previous PDF analyses, which artificially linked $s(x, Q)$ to the combination $(\bar{u} + \bar{d})$ of the lightest sea quarks.

The increased fractional uncertainty $\Delta r_{ZW}/r_{ZW}$ is related to weaker correlation between the CTEQ6.6 W and Z cross sections at the LHC. According to Eq. (10), $\Delta r_{ZW}/r_{ZW}$ scales approximately as $(1 - \cos\varphi)^{1/2}$, given that the W and Z fractional uncertainties are about the same ($\Delta\sigma_W/\sigma_W^0 \approx \Delta\sigma_Z/\sigma_Z^0$). The value of $\cos\varphi$ decreases from 0.998 in CTEQ6.1 to 0.956 in CTEQ6.6, or 0.982 if $s(x, Q)$ is fixed during the Hessian analysis at its best-fit CTEQ6.6M shape. As a result of the smaller $\cos\varphi$, $\Delta r_{ZW}/r_{ZW}$ increases threefold in the CTEQ6.6 prediction, even though the fractional uncertainties $\Delta\sigma_{W,Z}/\sigma_{W,Z}$ are reduced.

The eccentricity of the $\sigma_Z - \sigma_W$ tolerance ellipse grows with $\cos\varphi$, implying a narrow CTEQ6.1 ellipse and a broader CTEQ6.6 ellipse shown in Fig. 10. The CTEQ6.6 ellipse narrows if the strangeness parameters are fixed at their best-fit values as described above. Very different values of r_{ZW} can be obtained if one allows for the intrinsic charm contribution. In Fig. 10, the empty triangles correspond to the "maximal" intrinsic charm scenarios. These cross sections lie on the boundary or outside of the CTEQ6.6 tolerance ellipse. They can be potentially ruled out by measuring r_{ZW} precisely at the Tevatron, as can be deduced from Fig. 6(b).

4. W^- vs W^+ cross sections

The charge dependence of weak boson production at the LHC is explored by plotting W^- vs W^+ cross sections in

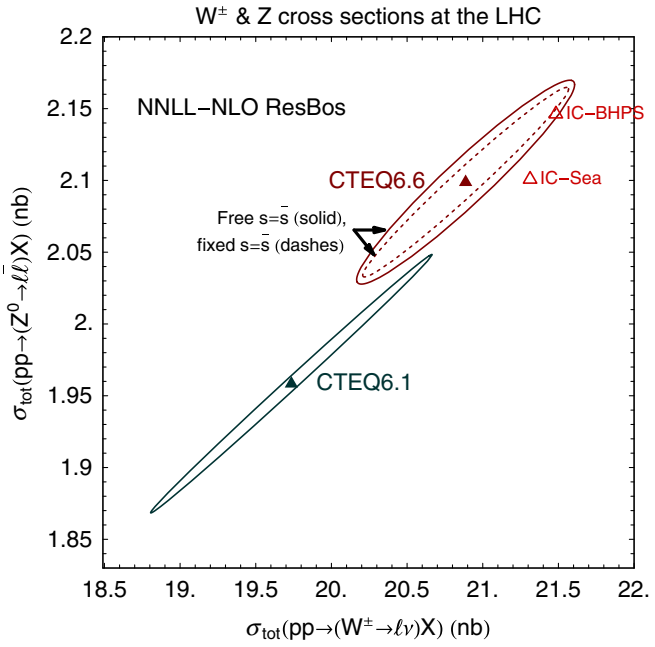

FIG. 10 (color online). W and Z correlation ellipses at the LHC obtained in the fits with free and fixed strangeness, as well as with maximal intrinsic charm contribution.

Fig. 11(a). In this case, the CTEQ6.6 prediction agrees well with the latest MSTW and AMP sets, while more substantial differences exist with the earlier MRST and ZEUS PDF sets. Possible intrinsic charm contributions (indicated by the IC-BHPS and IC-Sea points) would increase both cross sections.

The cross section ratio $\sigma_{W^-}/\sigma_{W^+}$ is most correlated with the valence u-quark PDF $u_V = u - \bar{u}$ at $Q = 85$ GeV, followed by the valence d-quark (cf. Fig. 11 (b)). There is a large correlation with $u_V(x, Q)$ at $x \approx 0.1$ and anticorrelation at $x \approx 0.05$. Other PDF flavors do not demonstrate pronounced correlation with $\sigma_{W^-}/\sigma_{W^+}$ and are not shown in the figure.

C. Top-quark production and gluon uncertainty

The prominent role of gluons in driving the PDF uncertainty in many processes has been pointed out in the past by noticing that most of the PDF uncertainty is often generated by a certain PDF eigenvector sensitive to the gluon parameters. While the abstract eigenvectors give largely a qualitative insight, the correlation analysis relates the PDF uncertainty directly to parton distributions for physical flavors at known (x, μ). We will now apply the correlation technique to investigate the uncertainties associated with gluons and heavy quarks in two other prominent processes, production of top-quark–antiquark pairs and single-top quarks.

1. Parametrization of $t\bar{t}$ and single-t total cross sections

The inclusive rate for production of top-quark–antiquark pairs, $p\overset{(-)}{p} \to t\bar{t}X$, is measured with good precision in the Tevatron Run-2. An even more precise measurement is possible with the large event yield expected at the LHC. Such a measurement can test the perturbative QCD prediction and provide an alternative method to determine the

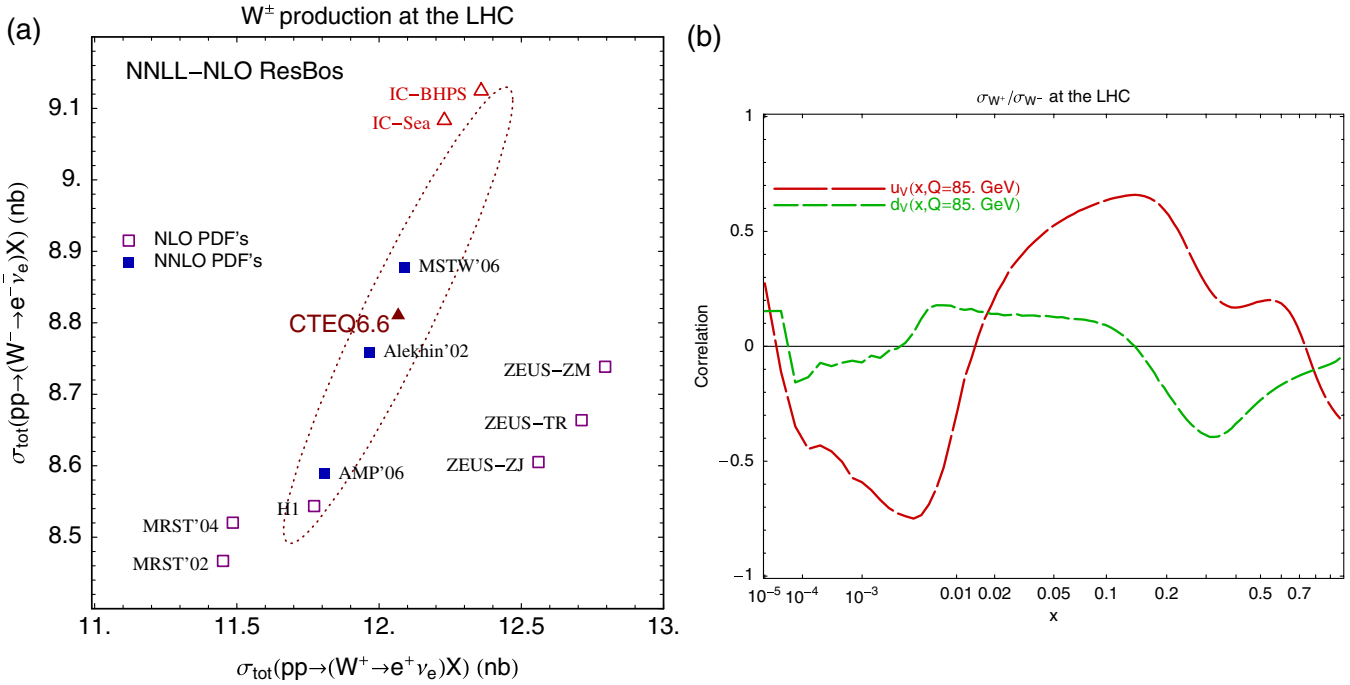

FIG. 11 (color online). (a) CTEQ6.6 W^- and W^+ production cross sections at the LHC compared with predictions for other PDF sets; (b) correlation $(\cos\varphi)$ between the ratio $\sigma_{W^+}/\sigma_{W^-}$ of W^+ and W^- total cross sections and valence quark PDFs.

mass of the top quark [71,72]. At leading order, $t\bar{t}$ pairs are produced via $q\bar{q}$ scattering (contributing 85% of the rate at the Tevatron) and gg scattering (contributing 90% of the rate at the LHC). At NLO, both the fixed-order [73–76] and resummed [72,77–88] cross sections have been computed. In this study, we calculate the NLO $t\bar{t}$ cross section using CTEQ6.6 PDFs and the MCFM code [34–36], for three values of the factorization scale ($\mu = 0.5m_t$, m_t, and $2m_t$).

Production of single-top quarks $p^{(-)}\bar{p} \to t^{\pm}X$ [89–109] provides a unique means to measure the Wtb coupling with the goal of constraining new physics [91,110–113]. It was recently observed for the first time by the Tevatron D0 [114] and CDF Collaborations [115]. We will focus on two single-top production channels, proceeding through t-channel and s-channel exchanges of charged weak (W) bosons. The t-channel W exchange involves bottom-quark scattering $qb \to q't$ and dominates both the Tevatron and LHC rates. The s-channel W exchange is similar to conventional W boson production, but occurs at larger typical x values (of the order $m_t/\sqrt{s}$ rather than $M_W/\sqrt{s}$). It may be observable at the Tevatron, but has a relatively small event rate at the LHC. We compute the NLO cross sections for single-top production using the programs from Refs. [103–107].

For each scale μ, we parametrize the resulting cross sections in the vicinity of the world-average top mass $m_t = 171 \pm 1.1(\text{stat}) \pm 1.5(\text{syst})$ GeV [116] by a function

$$\sigma(m_t, \mu) = A(\mu) + B(\mu)(m_t - 171) + C(\mu)(m_t - 171)^2, \quad (11)$$

where the units of σ and m_t are picobarn and GeV. The variation with respect to the reference cross section (corresponding to $\mu = m_t$) gives the NLO scale dependence $\Delta_\mu(m_t)$, discussed in detail in Sec. IV D. The uncertainty in σ due to the variation of m_t within the experimentally allowed range gives the mass dependence, denoted by Δ_m. We also calculate the relative PDF uncertainties, denoted by $\Delta_{\text{PDF}}(m_t)$. The values of Δ_μ, Δ_{PDF}, and coefficients A, B, C are listed in Table II. In single-top cross sections, we set $C = 0$. A plot of this parametric dependence in $t\bar{t}$ production at the Tevatron and LHC is shown in Fig. 12. The correlation cosines between $t\bar{t}$, single-top, W, and Z cross sections are listed in Tables I and III.

2. PDF-induced correlations

The PDF dependence of the top-quark cross sections follows a few nontrivial trends, which can be understood by studying x-dependent correlations between the top-quark cross sections and PDFs presented in Fig. 13. Our discussion will also refer to Tables I, II, and III.

(1) Contrary to the naive expectation, the main PDF uncertainty in $t\bar{t}$ production at the Tevatron is not associated with the leading $q\bar{q}$ scattering channel. Rather, the uncertainty is mostly correlated with the gluon PDF probed at $x \approx 0.3$, as clearly shown by the $t\bar{t}$-PDF correlations in Fig. 13(a). At such x values, the quark PDFs are tightly constrained, resulting in a small uncertainty in the leading $q\bar{q}$ channel, while the gluons are poorly known, resulting in a very large uncertainty in the subleading gg channel. The net result is a substantial total PDF uncertainty, $\Delta_{\text{PDF}} = 7.4\%$, in the Tevatron $t\bar{t}$ cross section, contributed mostly by gg scattering. By the momentum sum rule, the Tevatron $t\bar{t}$ cross section is strongly anticorrelated with gluon scattering at $x \sim 0.05$. It does not exhibit a strong (anti)correlation with W or Z production at either collider; cf. Table I.

(2) The Tevatron t-channel single-top cross section is mostly correlated with the b-quark PDF at $x \sim 0.2$,

TABLE II. The fitting parameters (A, B, C) for the parametric form (11) of the CTEQ6.6M total cross section for inclusive $t\bar{t}$ and single-top production at the Tevatron and LHC, evaluated at NLO in the QCD coupling strength. Also shown are the relative scale and PDF errors, Δ_μ and Δ_{PDF} at $m_t = 171$ GeV.

Final state	Parameter	$p\bar{p} \to TX$ ($\sqrt{s} = 1.96$ TeV) $\mu = m_t/2$	$\mu = m_t$	$\mu = 2m_t$	$pp \to TX$ ($\sqrt{s} = 14$ TeV) $\mu = m_t/2$	$\mu = m_t$	$\mu = 2m_t$
$T = t\bar{t}$	A [pb]	7.546	7.197	6.412	951.2	857.9	761.6
	B [pb · GeV^{-1}]	−0.237	−0.225	−0.201	−26.12	−23.43	−20.81
	C [pb · GeV^{-2}]	0.0041	0.0039	0.0034	0.44	0.37	0.33
	$\Delta_\mu(m_t = 171)$	+5%	reference	−11%	+11%	reference	−11%
	$\Delta_{\text{PDF}}(m_t = 171)$		$^{+8.4}_{-6.4}$ (**7.4**)%			$^{+3.3}_{-3.2}$ (3.3)%	
$T = t$ (t-channel)	A [pb]	1.96	2.01	2.058	248	248.4	249.1
	B [pb · GeV^{-1}]	−0.034	−0.036	−0.037	−1.93	−2.19	−2.24
	$\Delta_\mu(m_t = 171)$	−2.7%	reference	2.6%	−1.6%	reference	2.4%
	$\Delta_{\text{PDF}}(m_t = 171)$		**10.3**%			3.2%	
$T = t$ (s-channel)	A [pb]	1.013	0.967	0.925	11.83	11.710	11.67
	B [pb · GeV^{-1}]	−0.025	−0.024	−0.023	−0.248	−0.247	−0.248
	$\Delta_\mu(m_t = 171)$	+5%	reference	−4%	+1.0%	reference	−0.4%
	$\Delta_{\text{PDF}}(m_t = 171)$		3.4%			3.0%	

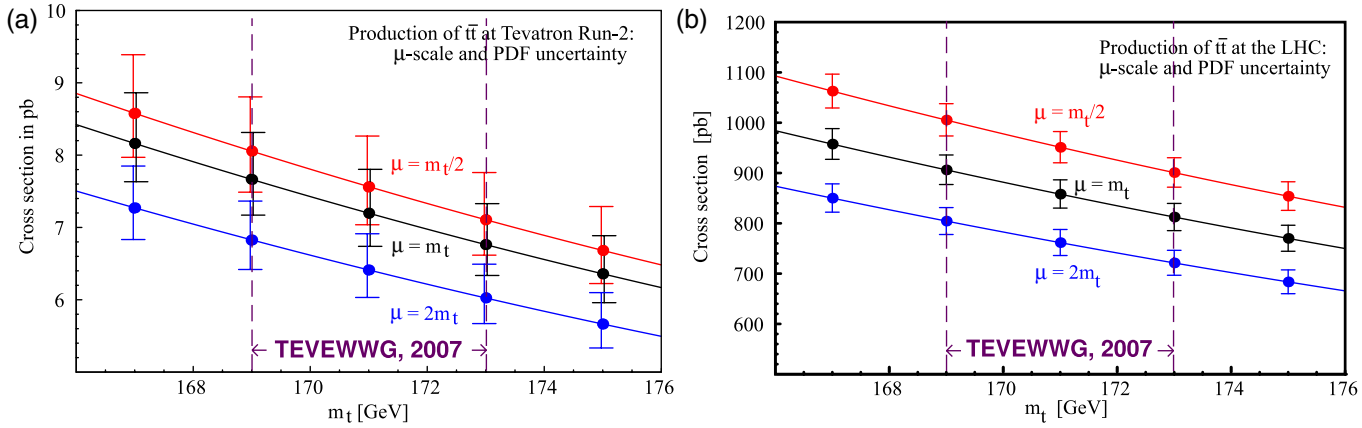

FIG. 12 (color online). CTEQ6.6 predictions for inclusive $t\bar{t}$ production at (a) the Tevatron Run-2 and (b) the LHC, showing the NLO cross section in pb versus the top-quark mass m_t. The three curves correspond to three choices for the factorization scale: $\mu = m_t/2$, m_t, and $2m_t$. The error bars are the PDF uncertainties. Also shown is the 1σ error range from the 2007 world-average experimental m_t value by the Tevatron Electroweak Working Group, $m_t = 171 \pm 1.1 \pm 1.5$ GeV [116].

as illustrated by Fig. 13(c). It has a substantial PDF uncertainty, $\Delta_{\rm PDF} = 10.3\%$. It is correlated with the Tevatron $t\bar{t}$ cross section ($\cos\varphi = 0.81$) and anticorrelated with Z, W production at the LHC ($\cos\varphi = -0.82$ and -0.79) through the shared correlation with the gluon at large x.

(3) At the LHC (Figs. 13(b) and 13(d)), the $t\bar{t}$ and t-channel single-top cross sections are also mostly correlated with g, c, and b PDFs, which, however, are well constrained at $x \sim 0.05$ and 0.01, typical values in this case. The PDF uncertainty is of the order 3% in both processes. The LHC $t\bar{t}$ cross sections are anticorrelated with the Z and W cross sections. The $t\bar{t} - Z$ and $t\bar{t} - W$ correlation cosines are large and negative: $\cos\varphi = -0.8$ and -0.74, respectively. The strong anticorrelation reveals itself in the shape of the $t\bar{t} - Z$ ellipse, plotted in Fig. 14 by using the PDF error parameters in Table I. A similar anticorrelation exists between the $t\bar{t}$ and W cross sections [117]. Interestingly enough, the LHC t-channel single-top cross section is only mildly anticorrelated with $t\bar{t}$ production and mildly correlated with W and Z production (see Table III), in contrast to the Tevatron.

(4) At both colliders, the s-channel PDF uncertainty is of the order 3% and correlated mostly with $\overset{(-)}{u}$ and $\overset{(-)}{d}$ PDFs (cf. Figs. 13(e) and 13(f)), as well as with the Tevatron Z, W rates. Remarkably, the LHC s-channel single-top cross section is not particularly correlated with the LHC W, Z cross sections, despite its similarities with W boson production. This peculiarity is due to large x values ($x \sim m_t/\sqrt{s} \sim 0.01$) typical for the s-channel single-top production. At such x, charm and bottom initial-state contributions are relatively small and do not affect single-top production as much as W boson production, hence preventing the gluon-driven PDF uncertainty from contributing sizably to the s-channel cross section.

(5) The improved evaluation of heavy-quark terms in the CTEQ6.6 PDFs reduces the Tevatron (LHC) $t\bar{t}$ cross sections by 4% (3.5%) compared to CTEQ6.1. The CTEQ6.6 Tevatron t-channel single-top cross section is about 6% smaller than the CTEQ6.1 cross section. The other three CTEQ6.6 single-top cross sections differ from the CTEQ6.1 cross sections by less than 2%.

D. $t\bar{t}$ production as a standard candle; Higgs boson production

To recap the previous section, at the Tevatron, $t\bar{t}$ production is strongly correlated with single-top production.

TABLE III. Correlation cosines $\cos\varphi$ between single-top, W, Z, and $t\bar{t}$ cross sections at the Tevatron Run-2 (Tev2) and LHC, computed with CTEQ6.6 PDFs.

Single-top production channel	Correlation $\cos\varphi$ with					
	Z^0 (Tev2)	$W^\pm$ (Tev2)	$t\bar{t}$ (Tev2)	Z^0 (LHC)	$W^\pm$ (LHC)	$t\bar{t}$ (LHC)
t-channel (Tev2)	−0.18	−0.22	**0.81**	**−0.82**	**−0.79**	0.56
t-channel (LHC)	0.09	0.14	−0.64	0.56	0.53	−0.42
s-channel (Tev2)	**0.83**	**0.79**	0.18	0.22	0.27	−0.3
s-channel (LHC)	**0.81**	**0.85**	−0.42	0.6	0.68	−0.33

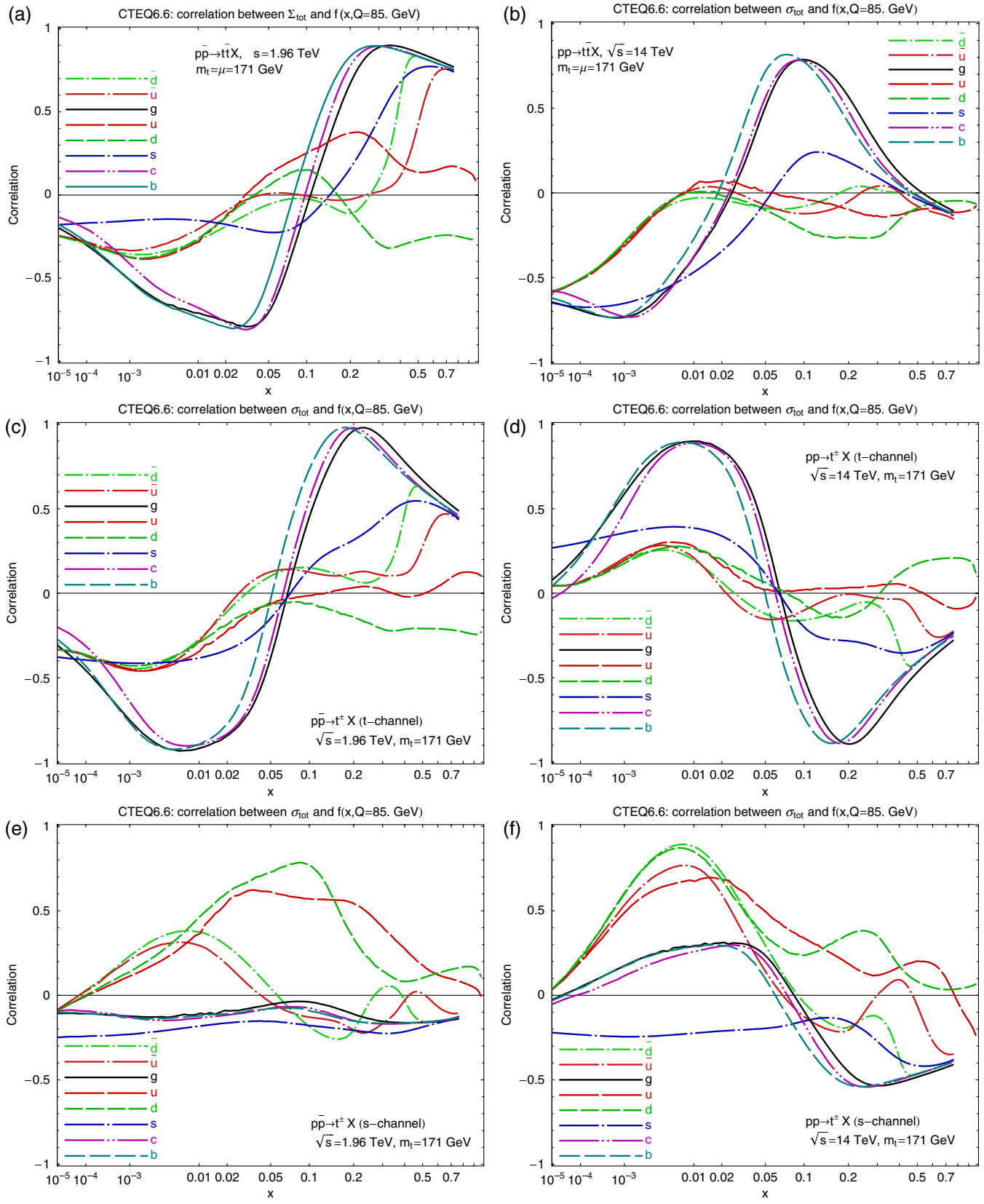

FIG. 13 (color online). PDF-induced correlations ($\cos\varphi$) between the total cross sections for $t\bar{t}$ and single-top production, and PDFs of various flavors, plotted as a function of x for $Q = 85$ GeV: Tevatron Run-2 (left column); LHC (right column).

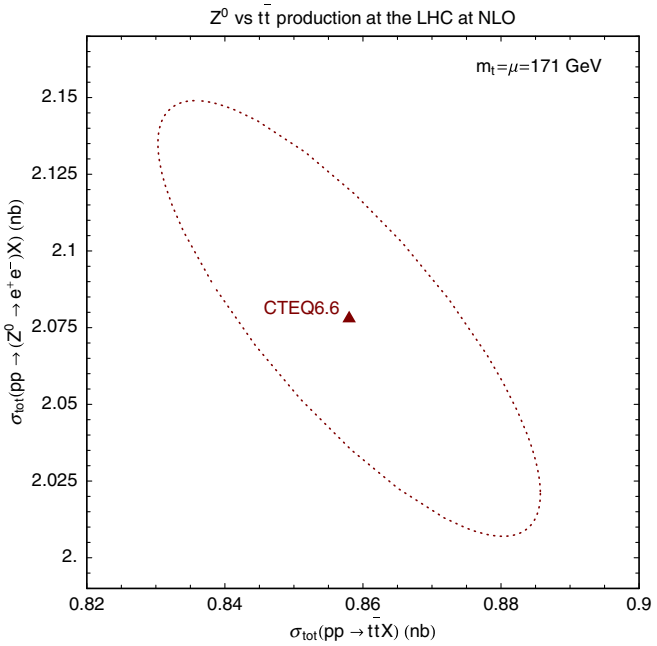

FIG. 14 (color online). Correlation ellipse for $t\bar{t}$ and Z boson NLO total cross sections at the LHC.

At the LHC, it is strongly anticorrelated with Z, W production. Precise measurements of $t\bar{t}$ rates could provide valuable constraints on the gluon and heavy-quark PDFs, if the associated theoretical and experimental uncertainties are each reduced below 3–5%. These measurements would help bring down the PDF error in many processes and supply an alternative way to monitor the collider luminosity. If a cross section is anticorrelated with W and Z production, it could be normalized to the $t\bar{t}$ cross section. The PDF error will be suppressed in such a cross section ratio, in contrast to the ratio with the W or Z cross section. Other systematic errors may cancel better, too, if the process shares common elements with $t\bar{t}$ production.

Let us consider some specific examples. The PDF uncertainties for Z, $W^{\pm}$, $t\bar{t}$, and Higgs boson (h^0) production via gluon fusion at the LHC, with Higgs mass $m_h = 500$ GeV, are 3.4%, 3.5%, 3.2%, and 4%, respectively. The correlation cosines are 0.956 for Z and $W^{\pm}$ cross sections, 0.98 for h^0 and $t\bar{t}$ cross sections, and -0.87 for h^0 and Z cross sections. By Eq. (10) the PDF uncertainty on the $Z/W^{\pm}$, $h^0/t\bar{t}$, h^0/Z cross section ratios are 1.3%, 1.5%, and 7.2%, i.e., the correlated cross sections produce ratios with the smallest PDF uncertainties.

The viability of precise $t\bar{t}$ production measurements can be examined by studying theoretical uncertainties on the $t\bar{t}$ cross section presented in Table II. At present, the scale dependence Δ_μ is larger than the PDF uncertainty $\Delta_{\rm PDF}$ and top-mass uncertainty Δ_m at both colliders, suggesting that higher-order (NNLO) corrections have a tangible impact on the $t\bar{t}$ rate.[7] The NNLO contributions will be computed in the near future [118], which will likely reduce the associated uncertainty to a few percent.

The top-mass uncertainty Δ_m can be brought down to 2–3% by measuring m_t with an accuracy of the order 1 GeV, as planned by the Tevatron experiments. Further advancements can possibly improve accuracy in the treatment of heavy-quark mass effects at NNLO to about a percent level. The current (not related to the luminosity) experimental systematic error for the $t\bar{t}$ cross section at the Tevatron is 8% [119], with further improvements likely. A similar systematic error of the order 5% may be feasible at the LHC.

The complementarity of constraints on Higgs boson searches from $t\bar{t}$ production at the LHC and Z boson production at the Tevatron and LHC is illustrated by Fig. 15, showing the correlation cosines ($\cos\varphi$) between Higgs, Z, and $t\bar{t}$ production cross sections as a function of Higgs mass. These cosines are shown by lines, in addition to separate markers corresponding to correlations between W, Z, and top production processes discussed above. The relevant cross sections are collected in Table I for W, Z, and $t\bar{t}$ production, and in Table IV for Higgs production processes.

As discussed earlier, there is a very large correlation between Z boson, W^+ boson, and W^- boson production at the LHC, and a strong anticorrelation between Z boson and $t\bar{t}$ production. Only a mild correlation exists between Z production at the Tevatron and Z production at the LHC. There is a moderate correlation between Z production and the production of a light (120 GeV) Higgs boson through gg fusion, but this becomes a strong anticorrelation as the mass of the Higgs boson increases, as the gluons are in a similar x range as those responsible for $t\bar{t}$ production. Associated Higgs boson production (Wh^0) is strongly correlated with Z production for low Higgs masses but becomes decorrelated for higher masses.[8] There is only a mild correlation between the production of a Higgs boson through vector boson fusion and Z production over a wide range of m_h.

The correlation curves with respect to $t\bar{t}$ production basically form a mirror image to the previous curves, since $t\bar{t}$ pairs at the LHC are predominantly produced via gg fusion at large x. Thus, for example, the production of a

[7]The scale dependence of the NLO $t\bar{t}$ cross section may be reduced by threshold resummation [72,82,83,88], which includes higher-order logarithmic terms that enforce renormalization group invariance. In our study, the scale dependence is viewed as an estimate of all NNLO contributions, including potentially sizable higher-order terms not associated with the threshold logarithms. A more conservative estimate of full NNLO effects is provided by the scale dependence of the fixed-order NLO cross section (11), rather than that of the threshold-resummed NLO cross section.

[8]Similarly, Wh^0 associated production ($m_h < 200$ GeV) and Z boson production are strongly correlated at the Tevatron.

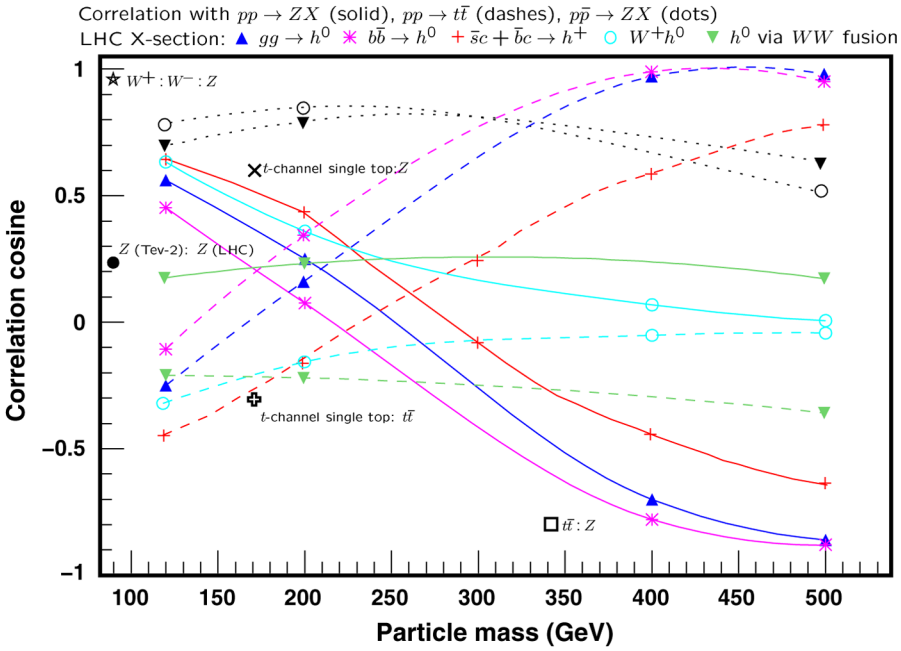

FIG. 15 (color online). The correlation cosine $\cos\varphi$ for Higgs boson searches at the LHC with respect to Z boson production at the LHC (solid line) and Tevatron (dotted line), and $t\bar{t}$ production at the LHC (dashed line), plotted as a function of Higgs mass. Separate markers denote correlations of W, t-channel single-top cross sections at the LHC and Z cross section at the Tevatron with respect to Z and $t\bar{t}$ cross sections at the LHC.

Higgs boson through gg fusion goes from a mild anticorrelation with $t\bar{t}$ for low Higgs masses to a high correlation for large Higgs masses.

PDF-induced correlations may follow a different pattern in other two-Higgs doublet models (2HDM). For example, the MSSM Higgs boson production $c\bar{s} + c\bar{b} \to h^+$ is not particularly correlated with $t\bar{t}$ production at $m_h \gtrsim 500$ GeV because of the uncorrelated contribution from the antistrangeness PDF (cf. Fig. 15). The $c\bar{s} \to h^+$ channel is absent in other 2HDM, such as the effective weak-scale 2HDM induced by top-color dynamics [120], where the scattering proceeds entirely via $c\bar{b} \to h^+$ at the Born level. In those models the correlation of the $t\bar{t}$ cross section with the h^+ cross section is very strong at large m_h ($\cos\varphi = 0.98$ for $m_h = 500$ GeV).

Higgs boson production at the LHC is affected by the new features of CTEQ6.6 PDFs in several ways. Table V lists the relative difference $\Delta_{\rm GM} \equiv \sigma_{6.1}/\sigma_{6.6} - 1$ between the CTEQ6.1 and CTEQ6.6 cross sections, as well as CTEQ6.6 PDF uncertainties $\Delta_{\rm PDF}$ for Higgs boson production in a mass range $m_h = 100$–800 GeV. In processes dominated by light-quark scattering (vector boson fusion, $W^\pm h$, $Z^0 h$, and $Ah^\pm$), the most tangible differences between CTEQ6.6 and CTEQ6.1 (compared to the PDF uncertainty) occur at m_h of the order 100 GeV, where $\Delta_{\rm GM}$ is close in magnitude to $\Delta_{\rm PDF}$, reflecting the enhancement in CTEQ6.6 u and d PDFs at $x = 10^{-3}$–10^{-2}. In gluon-gluon fusion $gg \to h$, the difference between CTEQ6.6 and 6.1 is well within the PDF uncertainty ($\Delta_{\rm GM} < \Delta_{\rm PDF}$), although $\Delta_{\rm GM}$ becomes comparable to $\Delta_{\rm PDF}$ for heavy Higgs masses ($m_h \gtrsim 500$ GeV). Similarly, $\Delta_{\rm GM}$ is smaller than $\Delta_{\rm PDF}$ in heavy-quark scattering $c\bar{b} \to h^+$. The most striking differences occur in $c\bar{s} \to h^+$, because the CTEQ6.1 and CTEQ6.6 strangeness

TABLE IV. CTEQ6.6M total cross sections σ and PDF errors $\Delta\sigma$ for Higgs boson production at $\sqrt{s} = 14$ TeV shown in Fig. 15.

Scattering process	σ and $\Delta\sigma$ (pb)		
	$m_h = 120$ GeV	$m_h = 200$ GeV	$m_h = 500$ GeV
$pp \to (gg \to h^0)X$	33(1)	14.0(4)	4.0(2)
$pp \to (b\bar{b} \to h^0)X$	2750(130)	460(20)	11.0(7)
$pp \to (c\bar{s} + c\bar{b} \to h^+)X$	16(1)	2.61(14)	0.063(3)
$pp \to W^+h^0X$	1.15(3)	0.201(6)	0.0062(3)
$pp \to W^-h^0X$	0.74(2)	0.117(4)	0.002 92(16)
$pp \to (WW \to h^0)X$	2.80(8)	1.60(5)	0.36(1)

TABLE V. Relative differences $\Delta_{GM} \equiv \sigma_{6.1}/\sigma_{6.6} - 1$ between CTEQ 6.1 and CTEQ 6.6 cross sections for Higgs boson production at the LHC listed at the beginning of Sec. IV, compared to the PDF uncertainties Δ_{PDF} in these processes. The $Ah^{\pm}$ cross section is for combined production of positively and negatively charged Higgs bosons, with m_h being the mass of the CP-odd boson ($m_h = m_A$), and $m_{h^{\pm}}$ given by $m^2_{h^{\pm}} = m^2_A + M^2_W$.

m_h (GeV)	$\Delta_{GM}(\%)\|\Delta_{PDF}(\%)$													
	VBF		Z^0h		$Ah^{\pm}$		$gg \to h$		$c\bar{b} \to h^+$		$c\bar{s} \to h^+$		$c\bar{s} + c\bar{b} \to h^+$	
100	**−3.8**	**3.1**	**−3.2**	**2.7**	**−3.2**	**4.3**	0.6	4.4	1.5	5.9	**−18**	**10**	**−8.4**	**6.9**
200	−1.8	2.8	−1.6	2.8	−1.9	4.3	1.7	3.2	2.1	4.7	**−16**	**8**	**−6.6**	**5.4**
300	−1.6	2.8	−0.6	3	−0.4	5.3	2.3	2.7	1.9	4.3	**−14**	**7**	**−6.2**	**4.5**
400	−0.1	3.3	0	3.4	0.7	6.6	2.8	3.8	2	4.8	**−13**	**6.3**	**−5.6**	**4.4**
500	0.2	2.8	0.4	3.7	1.1	7.6	3.3	3.9	2.3	6.1	**−12**	**6.3**	**−5**	**5.1**
600	−0.7	3.5	0.7	4.1	1.6	9.2	3.8	5.0	2.8	8	**−11**	**6.8**	−4.2	6.4
700	0.2	3.0	0.9	4.4	2.1	11	4.3	6.3	3.4	10	**−9.9**	**7.7**	−3.4	8
800	2.3	3.5	1	4.8	2.8	13	4.9	7.8	4.1	12	**−8.7**	**9**	−2.4	10

distributions disagree by a large amount in most of the x range.

V. CONCLUSION

The new CTEQ6.6 global analysis incorporates the latest improvements in the perturbative QCD treatment of s, c, and b quark PDFs introduced in Refs. [5–7]. It predicts substantial modifications (comparable to, or exceeding in magnitude the NNLO contributions) in high-energy electroweak precision cross sections, notably 6–7% enhancements in W and Z cross sections at the LHC above the predictions in the zero-mass scheme. Theoretical improvements of this kind must be accompanied by the development of efficient strategies to understand and reduce the remaining uncertainties in the PDF parameters. This work presents a novel correlation analysis, a technique based on the Hessian method that links the PDF uncertainty in a hadronic cross section to PDFs for *physical* parton flavors at well-defined (x, μ) values.

We apply the correlation analysis to reveal and explain several regularities observed in the PDF dependence, such as strong sensitivity of W, Z production at the LHC and $t\bar{t}$ production at the Tevatron (processes dominated by $q\bar{q}$ scattering) to uncertainties in the gluon and heavy-quark PDFs; the leading role played by the strangeness distribution $s(x, \mu)$ in the PDF uncertainty of the ratio $r_{ZW} = \sigma_Z/\sigma_W$ of the LHC Z and W cross sections; and intriguing PDF-induced anticorrelations between the LHC Z, W cross sections and processes dominated by large-x gluon scattering, such as heavy Higgs boson production via gluon fusion. Similarities and differences in the correlations between the physical Z, W, $t\bar{t}$ cross sections and PDFs of various flavors reflected in Figs. 8, 9, and 13 provide explicit guidance for reducing the theoretical uncertainty due to the PDF dependence in upcoming measurements of W boson and top-quark masses, and in the monitoring of the LHC luminosity in Z boson production.

In our study, we identify pairs of hadronic cross sections with strongly correlated or anticorrelated PDF dependence, i.e. with the correlation cosine $\cos\varphi$ close to 1 or -1. Such pairs are especially helpful for constraining the PDF uncertainties, in view that a combination of the existing CTEQ6.6 and upcoming LHC constraints on one cross section in the pair is guaranteed to substantially reduce the PDF uncertainty on the second cross section [cf. the discussion accompanying Eq. (9)]. In addition, ratios of correlated (but not anticorrelated) cross sections have greatly reduced PDF uncertainty, as follows from Eq. (11). For this reason, it is beneficial to normalize an LHC cross section to a standard-candle cross section with which it has a large PDF-induced correlation.

We point out a potentially valuable role of precise measurements of $t\bar{t}$ cross sections at the Tevatron and LHC for constraining the gluon PDF at large x and normalizing the LHC cross sections that are anticorrelated with W and Z boson production. If both theoretical and experimental uncertainties on $t\bar{t}$ cross sections are reduced to a level of 3–5%, as may become possible in the near future, the $t\bar{t}$ cross sections would provide an additional standard-candle observable with useful complementarity to Z and W boson cross sections. These measurements will be essential for reducing theoretical uncertainties in single-top and Higgs boson production, and for constructing cross section ratios with small PDF uncertainties.

ACKNOWLEDGMENTS

We thank J. Smith for providing a computer program to verify the $t\bar{t}$ production cross sections; A. Cooper-Sarkar, N. Kidonakis, M. Mangano, J. Stirling, and CTEQ members for helpful communications; and E. L. Berger for the critical reading of the manuscript. We are especially grateful to R. Thorne for a valuable comment about the strangeness distribution at small x that resulted in improvements in the revised paper, and for other discussions. This work was supported in part by the U.S. National Science Foundation under Grants No. PHY-0354838, No. PHY-0555545, and No. PHY-0551164; by the U.S. Department of Energy under Grant No. DE-FG03-94ER40837; and by

the National Science Council of Taiwan under Grant No. NSC-95-2112-M-133-001. The work of P. M. N. on an early version of the manuscript at the Argonne National Laboratory was supported by the U.S. Department of Energy, Division of High Energy Physics, under Contract No. DE-AC02-06CH11357. P. M. N. acknowledges the hospitality of the Kavli Institute for Theoretical Physics at the University of California in Santa Barbara during the final stage of this work.

[1] M. Dittmar, F. Pauss, and D. Zurcher, Phys. Rev. D **56**, 7284 (1997).
[2] V. A. Khoze, A. D. Martin, R. Orava, and M. G. Ryskin, Eur. Phys. J. C **19**, 313 (2001).
[3] W. T. Giele and S. A. Keller, arXiv:hep-ph/0104053.
[4] H. J. Frisch, CDF Public Note No. 2484, 1994.
[5] W.-K. Tung *et al.*, J. High Energy Phys. 02 (2007) 053.
[6] H. L. Lai *et al.*, J. High Energy Phys. 04 (2007) 089.
[7] J. Pumplin, H. L. Lai, and W.-K. Tung, Phys. Rev. D **75**, 054029 (2007).
[8] J. Pumplin *et al.*, J. High Energy Phys. 07 (2002) 012.
[9] D. Stump *et al.*, J. High Energy Phys. 10 (2003) 046.
[10] J. Pumplin *et al.*, Phys. Rev. D **65**, 014013 (2001).
[11] P. M. Nadolsky and Z. Sullivan, arXiv:hep-ph/0110378.
[12] J. C. Collins, Phys. Rev. D **58**, 094002 (1998).
[13] M. A. G. Aivazis, J. C. Collins, F. I. Olness, and W.-K. Tung, Phys. Rev. D **50**, 3102 (1994).
[14] M. Kramer, F. I. Olness, and D. E. Soper, Phys. Rev. D **62**, 096007 (2000).
[15] W.-K. Tung, S. Kretzer, and C. Schmidt, J. Phys. G **28**, 983 (2002).
[16] http://projects.hepforge.org/lhapdf/.
[17] http://hep.pa.msu.edu/cteq/public/6.6/pdfs/.
[18] M. Tzanov *et al.* (NuTeV Collaboration), Phys. Rev. D **74**, 012008 (2006).
[19] S. J. Brodsky, P. Hoyer, C. Peterson, and N. Sakai, Phys. Lett. **93B**, 451 (1980).
[20] http://hep.pa.msu.edu/cteq/public/6.6/pdfcorrs/.
[21] R. Brock *et al.*, arXiv:hep-ex/0011009.
[22] S. Rajagopalan and M. Rijssenbeek, in Proceedings of 1996 DPF/DPB Summer Study on New Directions for High-Energy Physics (Snowmass 96), Snowmass, Colorado, 1996, p. LTH091 (available at http://www.slac.stanford.edu/econf/C960625/).
[23] W. T. Giele and S. Keller, Phys. Rev. D **57**, 4433 (1998).
[24] D. Shpakov, Ph.D. thesis, Stony Brook, 2000.
[25] M. Spira, arXiv:hep-ph/9510347.
[26] M. Spira, Fortschr. Phys. **46**, 203 (1998).
[27] J. L. Diaz-Cruz, H.-J. He, and C.-P. Yuan, Phys. Lett. B **530**, 179 (2002).
[28] S. Kanemura and C.-P. Yuan, Phys. Lett. B **530**, 188 (2002).
[29] Q.-H. Cao, S. Kanemura, and C.-P. Yuan, Phys. Rev. D **69**, 075008 (2004).
[30] LEP Higgs Working Group, arXiv:hep-ex/0107030.
[31] S. Berge, P. M. Nadolsky, and F. I. Olness, Phys. Rev. D **73**, 013002 (2006).
[32] A. Belyaev, P. M. Nadolsky, and C.-P. Yuan, J. High Energy Phys. 04 (2006) 004.
[33] C.-P. Yuan and collaborators (unpublished).
[34] J. Campbell, R. K. Ellis, and F. Tramontano, Phys. Rev. D **70**, 094012 (2004).
[35] J. Campbell and F. Tramontano, Nucl. Phys. **B726**, 109 (2005).
[36] J. M. Campbell and R. K. Ellis, Phys. Rev. D **62**, 114012 (2000).
[37] R. Hamberg, W. L. van Neerven, and T. Matsuura, Nucl. Phys. **B359**, 343 (1991); **B644**, 403(E) (2002).
[38] R. V. Harlander and W. B. Kilgore, Phys. Rev. Lett. **88**, 201801 (2002).
[39] C. Anastasiou, L. Dixon, K. Melnikov, and F. Petriello, Phys. Rev. D **69**, 094008 (2004).
[40] C. Anastasiou, L. J. Dixon, K. Melnikov, and F. Petriello, Phys. Rev. Lett. **91**, 182002 (2003).
[41] G. A. Ladinsky and C.-P. Yuan, Phys. Rev. D **50**, R4239 (1994).
[42] C. Balazs and C.-P. Yuan, Phys. Rev. D **56**, 5558 (1997).
[43] F. Landry, R. Brock, P. M. Nadolsky, and C.-P. Yuan, Phys. Rev. D **67**, 073016 (2003).
[44] H. L. Lai *et al.*, Phys. Rev. D **51**, 4763 (1995).
[45] H. L. Lai *et al.*, Phys. Rev. D **55**, 1280 (1997).
[46] H. L. Lai and W.-K. Tung, Z. Phys. C **74**, 463 (1997).
[47] H. L. Lai *et al.*, Eur. Phys. J. C **12**, 375 (2000).
[48] S. Kretzer, H. L. Lai, F. I. Olness, and W.-K. Tung, Phys. Rev. D **69**, 114005 (2004).
[49] S. Alekhin, Phys. Rev. D **68**, 014002 (2003).
[50] S. Alekhin, K. Melnikov, and F. Petriello, Phys. Rev. D **74**, 054033 (2006).
[51] C. Adloff *et al.* (H1 Collaboration), Eur. Phys. J. C **30**, 1 (2003).
[52] A. D. Martin, R. G. Roberts, W. J. Stirling, and R. S. Thorne, Eur. Phys. J. C **28**, 455 (2003).
[53] A. D. Martin, R. G. Roberts, W. J. Stirling, and R. S. Thorne, Eur. Phys. J. C **35**, 325 (2004).
[54] A. D. Martin, R. G. Roberts, W. J. Stirling, and R. S. Thorne, Phys. Lett. B **604**, 61 (2004).
[55] A. D. Martin, W. J. Stirling, R. S. Thorne, and G. Watt, Phys. Lett. B **652**, 292 (2007).
[56] S. Chekanov *et al.* (ZEUS Collaboration), Phys. Rev. D **67**, 012007 (2003).
[57] S. Chekanov *et al.* (ZEUS Collaboration), Eur. Phys. J. C **42**, 1 (2005).
[58] P. M. Nadolsky and C.-P. Yuan, Nucl. Phys. **B666**, 3 (2003).
[59] U. Baur, O. Brein, W. Hollik, C. Schappacher, and D. Wackeroth, Phys. Rev. D **65**, 033007 (2002).
[60] U. Baur, S. Keller, and D. Wackeroth, Phys. Rev. D **59**, 013002 (1998).
[61] A. Arbuzov *et al.*, Eur. Phys. J. C **54**, 451 (2008).
[62] J. H. Kuhn, A. Kulesza, S. Pozzorini, and M. Schulze,

Nucl. Phys. **B797**, 27 (2008).
[63] J. H. Kuhn, A. Kulesza, S. Pozzorini, and M. Schulze, Phys. Lett. B **651**, 160 (2007).
[64] C. M. Carloni Calame, S. Jadach, G. Montagna, O. Nicrosini, and W. Placzek, Acta Phys. Pol. B **35**, 1643 (2004).
[65] C. M. Carloni Calame, G. Montagna, O. Nicrosini, and A. Vicini, J. High Energy Phys. 12 (2006) 016.
[66] C. M. C. Calame, G. Montagna, O. Nicrosini, and A. Vicini, J. High Energy Phys. 10 (2007) 109.
[67] C. E. Gerber *et al.* (TeV4LHC Top and Electroweak Working Group), arXiv:0705.3251.
[68] Q.-H. Cao and C.-P. Yuan, Phys. Rev. Lett. **93**, 042001 (2004).
[69] S. Frixione and M. L. Mangano, J. High Energy Phys. 05 (2004) 056.
[70] F. Olness *et al.*, Eur. Phys. J. C **40**, 145 (2005).
[71] S. Frixione, M. L. Mangano, P. Nason, and G. Ridolfi, Phys. Lett. B **351**, 555 (1995).
[72] M. Cacciari, S. Frixione, M. L. Mangano, P. Nason, and G. Ridolfi, J. High Energy Phys. 04 (2004) 068.
[73] P. Nason, S. Dawson, and R. K. Ellis, Nucl. Phys. **B303**, 607 (1988).
[74] P. Nason, S. Dawson, and R. K. Ellis, Nucl. Phys. **B327**, 49 (1989); **B335**, 260(E) (1990).
[75] W. Beenakker, H. Kuijf, W. L. van Neerven, and J. Smith, Phys. Rev. D **40**, 54 (1989).
[76] W. Beenakker, W. L. van Neerven, R. Meng, G. A. Schuler, and J. Smith, Nucl. Phys. **B351**, 507 (1991).
[77] E. Laenen, J. Smith, and W. L. van Neerven, Nucl. Phys. **B369**, 543 (1992).
[78] E. Laenen, J. Smith, and W. L. van Neerven, Phys. Lett. B **321**, 254 (1994).
[79] E. L. Berger and H. Contopanagos, Phys. Lett. B **361**, 115 (1995).
[80] E. L. Berger and H. Contopanagos, Phys. Rev. D **54**, 3085 (1996).
[81] E. L. Berger and H. Contopanagos, Phys. Rev. D **57**, 253 (1998).
[82] S. Catani, M. L. Mangano, P. Nason, and L. Trentadue, Nucl. Phys. **B478**, 273 (1996).
[83] R. Bonciani, S. Catani, M. L. Mangano, and P. Nason, Nucl. Phys. **B529**, 424 (1998).
[84] N. Kidonakis and G. Sterman, Phys. Lett. B **387**, 867 (1996).
[85] N. Kidonakis and G. Sterman, Nucl. Phys. **B505**, 321 (1997).
[86] N. Kidonakis, Phys. Rev. D **64**, 014009 (2001).
[87] N. Kidonakis, E. Laenen, S. Moch, and R. Vogt, Phys. Rev. D **64**, 114001 (2001).
[88] N. Kidonakis and R. Vogt, Phys. Rev. D **68**, 114014 (2003).
[89] S. Dawson, Nucl. Phys. **B249**, 42 (1985).
[90] S. Willenbrock and D. Dicus, Phys. Rev. D **34**, 155 (1986).
[91] C.-P. Yuan, Phys. Rev. D **41**, 42 (1990).
[92] S. Cortese and R. Petronzio, Phys. Lett. B **253**, 494 (1991).
[93] R. K. Ellis and S. J. Parke, Phys. Rev. D **46**, 3785 (1992).
[94] T. Stelzer and S. Willenbrock, Phys. Lett. B **357**, 125 (1995).
[95] M. C. Smith and S. Willenbrock, Phys. Rev. D **54**, 6696 (1996).
[96] T. Stelzer, Z. Sullivan, and S. Willenbrock, Phys. Rev. D **56**, 5919 (1997).
[97] S. Mrenna and C.-P. Yuan, Phys. Lett. B **416**, 200 (1998).
[98] T. Stelzer, Z. Sullivan, and S. Willenbrock, Phys. Rev. D **58**, 094021 (1998).
[99] G. Bordes and B. van Eijk, Z. Phys. C **57**, 81 (1993).
[100] G. Bordes and B. van Eijk, Nucl. Phys. **B435**, 23 (1995).
[101] G. A. Ladinsky and C.-P. Yuan, Phys. Rev. D **43**, 789 (1991).
[102] S. Moretti, Phys. Rev. D **56**, 7427 (1997).
[103] B. W. Harris, E. Laenen, L. Phaf, Z. Sullivan, and S. Weinzierl, Phys. Rev. D **66**, 054024 (2002).
[104] Z. Sullivan, Phys. Rev. D **70**, 114012 (2004).
[105] Q.-H. Cao and C.-P. Yuan, Phys. Rev. D **71**, 054022 (2005).
[106] Q.-H. Cao, R. Schwienhorst, and C.-P. Yuan, Phys. Rev. D **71**, 054023 (2005).
[107] Q.-H. Cao, R. Schwienhorst, J. A. Benitez, R. Brock, and C.-P. Yuan, Phys. Rev. D **72**, 094027 (2005).
[108] N. Kidonakis, Phys. Rev. D **74**, 114012 (2006).
[109] N. Kidonakis, Phys. Rev. D **75**, 071501 (2007).
[110] T. Tait and C.-P. Yuan, Phys. Rev. D **63**, 014018 (2000).
[111] T. Tait and C.-P. Yuan, arXiv:hep-ph/9710372.
[112] D. Carlson, Ph.D. thesis, Michigan State University, 1995, arXiv:hep-ph/9508278.
[113] A. P. Heinson, A. S. Belyaev, and E. E. Boos, Phys. Rev. D **56**, 3114 (1997).
[114] V. M. Abazov *et al.* (D0 Collaboration), Phys. Rev. Lett. **98**, 181802 (2007).
[115] W. Wagner (CDF Collaboration), arXiv:0705.2954.
[116] Tevatron Electroweak Working Group, arXiv:hep-ex/0703034.
[117] J. M. Campbell, J. W. Huston, and W. J. Stirling, Rep. Prog. Phys. **70**, 89 (2007).
[118] M. Czakon, A. Mitov, and S. Moch, Nucl. Phys. **B798**, 210 (2008).
[119] CDF Collaboration, CDF Public Note No. 8148, 2006.
[120] C. Balazs, H.-J. He, and C.-P. Yuan, Phys. Rev. D **60**, 114001 (1999).